2016

A Biophysical Study of the Ion Transport Mechanism in Uncoupling Protein 2 by Investigating the Role of Lysine Residues in its Matrix Network

Stephanie O. Uwumarenogie
Wilfrid Laurier University, stephuw29@gmail.com

A Biophysical Study of the Ion Transport Mechanism in Uncoupling Protein 2 by Investigating the Role of Lysine Residues in its Matrix Network

By

Stephanie O. Uwumarenogie

B.Sc. Biochemistry, University of Waterloo, 2013

THESIS

Submitted to the Department of Chemistry and Biochemistry

In partial fulfilment of the requirements for

Master of Science in Chemistry

Wilfrid Laurier University

ABSTRACT

Uncoupling protein 2 (UCP2) is one of five UCP homologues found in the inner mitochondrial membrane that transports protons from the intermembrane space to the mitochondrial matrix. In turn, the proton motive force is dissipated and less ATP is produced in the mitochondria. UCP2 is proposed to influence insulin secretion in type II diabetes, and decrease the amount of reactive oxygen species produced in the mitochondria, however the detailed mechanism of ion (proton and anions) transport in UCP2 and other UCP homologues are not fully understood. Sequence alignment analysis performed on proteins in the mitochondrial carrier family (MCF) including UCPs, identified a matrix network of positively and negatively charged residues that were proposed to form salt bridges and mediate substrate translocation through the proteins. In this study, the positively charged lysine residues in the matrix network were investigated for their influence on the proton transport and nucleotide binding activity of UCP2. For this reason, four UCP2 mutants: K38Q, K141Q, K239Q, and K38Q/K239Q (double mutant) and native proteins were expressed in bacterial membranes. After which the conformation of the purified proteins was analyzed with far-UV circular dichroism (CD). Finally, a fluorescence-based assay was used to study the proton transport and nucleotide binding properties of the proteins. The overall conformations of the proteins were α-helical but the shifts in negative ellipticity at 208 nm and 222 nm observed for the mutants inferred a change in the helical packing of these proteins compared to the wild type. In addition, the mutant proteins had proton transport rates that were 35% (K38Q and K239Q) and 65% (K141Q and double mutant) less than the native UCP2. In the presence of ATP, the proton transport rates of the mutant proteins decreased by 3-6% except for K38Q that had a 38% decrease in proton transport activity. In summary, these results revealed that the positively charged lysine residues in the

matrix network could participate in a salt bridge interaction that regulates the degree of helical packing, the ion transport activity and nucleotide binding properties in UCP2.

ACKNOWLEDGEMENTS

I would like to both acknowledge and thank my supervisor Dr. Masoud Jelokhani-Niaraki for his suggestions, criticisms and support these past two years. He has without a doubt helped me become a better researcher and his support was invaluable in getting me to this point. His experience and advice during rougher times of the research was very much appreciated.

I would also like to acknowledge my committee members, Dr. Matt Smith, Dr. Geoff Horsman, and thank them not just for their criticism but more importantly, their advice on how best to move forward with research process. In particular, I would like to thank Dr. Matt Smith for granting me access to his laboratory equipment and his suggestions on molecular biology aspects and proton transport measurements of this project. I would like to thank Dr. Michael Suits for his help on using the PyMOL visualization tool.

I would like to thank all of the colleagues I have had the opportunity to work with in Dr. Jelokhani's and Dr. Smith's labs throughout the past two years of my graduate studies, namely: Tyler Auld and Tu Hoang for their friendship and technical support during his project, James Mori, Brittany Porter, Nick Grimberg, Emily Tran among others for their company and help. Specifically, I would like to thank Patrick Hoang, for his guidance and support in troubleshooting proton transport assay, and finally, I would like to thank my family and close friends for their immeasurable support and sacrifice these past two years. I do not think I could have made it without their constant support and belief in me.

DECLARATION OF WORK PERFORMED

All data presented and described in this thesis are the results of my own, Stephanie Uwumarenogie's, work.

TABLE OF CONTENTS

LIST OF TABLES

LIST OF FIGURES

ABBREVIATIONS

AAC	ADP/ATP carrier protein
ADP	Adenosine diphosphate
ATP	Adenosine triphosphate
BL21 CD^+	BL21-CodonPlus (DE3)-RIPL
C_8E_4	Tetraethylene glycol monooctyl ether
Cam	Chloramphenicol
CD	Circular Dichroism
DNA	Deoxyribonucleic acid
E.coli	*Escherichia coli*
ETC	Electron Transport Chain
FA	Fatty acids
FRET	Fluorescence Resonance Energy Transfer
HF	High Fidelity
His-tag	hexapolyhistidine tag
IMAC	Immobilized Metal Affinity Chromatography
IMS	Intermembrane Space
IMM	Inner Mitochondria Membrane
Kan	Kanamycin
LB	Luria-Bertani broth
LDAO	Lauryldimethylamine-oxide
MCF	Mitochondria Carrier Family
MW	Molecular weight
OG	Octyl Glucoside
OMM	Outer Mitochondria Membrane
PCR	Polymerase Chain Reaction
RBF	Round-bottom flask

SDS-PAGE	Sodium dodecyl sulfate polyacrylamide gel electrophoresis
SPQ	6-methoxy-N-(3-sulfopropyl) quinolinium
Strep	Streptomycin
THP	Tris(hydroxypropyl)phosphine
TM	Transmembrane
UCP2-WT	Wildtype Uncoupling Protein 2

CHAPTER 1: INTRODUCTION

1.1. Mitochondria and ATP Production

Mitochondria are membrane-bound organelles located in the cytoplasm of eukaryotic cells. In the mitochondria, energy derived from the oxidation of carbohydrates and fatty acids are converted into the cells energy currency known as adenosine triphosphate (ATP) [1]. ATP is used to drive many cellular functions, including, but not limited to, muscle contraction, cell division, signalling, protein folding, and protein degradation [1, 2].

The mitochondrion structure is composed of an outer mitochondrial membrane (OMM), an intermembrane space (IMS), an inner mitochondrial membrane (IMM) and a mitochondrial matrix (MM) (Figure 1 and 2) [2, 3]. The OMM separates the IMS from the cytosol and it's composed of 50% phospholipids and 50% proteins by weight. The OMM includes prions, which makes it permeable to small molecules like coenzyme Q and ATP [4]. Additionally, the IMM separates the IMS from the mitochondrial matrix and is less permeable to solutes and ions compared to the OMM. The IMM has a 25% phospholipid and 75% protein weight composition [4]. In comparison, the IMM has a higher cardiolipin (CL) content (20% of total lipid) than the OMM. The IMMs high CL content could lead to specific CL-protein interactions that may modulate the activity of certain proteins in the IMM including complexes in the electron transport chain [5], ATP/ADP carrier (AAC) [6], and uncoupling proteins (UCPs) [7]. The IMM is folded to form invaginations called cristae (Figure 1) [4]. These invaginations are proposed to increase the membrane surface area and ensure ATP synthase and protein complexes of the ETC are organized in the IMM to maximize ATP production [4]. Furthermore, cristae with large surface areas are abundant in the mitochondria of tissues with high respiration rates, such as muscle and neurons [4].

ATP is produced in the mitochondria through the process of oxidative phosphorylation. More specifically, the oxidation of energy-rich compounds such as carbohydrates and fatty acids (FAs) results in the reduction of NAD^+ and FAD into NADH and $FADH_2$ [4]. These reduced electron carriers supply their electrons to protein complexes in the electron transport chain (ETC). The ETC is composed of: NADH dehydrogenase (complex I), succinate dehydrogenase (complex II), cytochrome c reductase (complex III), and cytochrome oxidase (complex IV) [8]. The movement of electrons through these complexes ETC results in the reduction of oxygen to water and pumping of protons (by complexes I, III, and IV) from the matrix into the intermembrane space [8]. This proton pumping enhanced an electrochemical gradient (proton motive force (PMF)) across the IMM that is the driving force for transporting the protons back into the matrix through the F_0F_1 ATP synthase. The dissipation of the PMF through ATP synthase provides the energy for this complex protein to synthesize ATP from adenosine diphosphate (ADP) and inorganic phosphate (P_i) (Figure 2) [8].

The PMF generated by the ETC is also dissipated by other proteins in the IMM, resulting in uncoupling the ETC from ATP synthesis. The uncoupling effect accounts for 25% basal metabolic rate and can be mediated through several proteins such as the phosphate transporter, glutamate carrier, AAC, and uncoupling proteins (UCPs) [4, 8]. In brown adipose tissues (BAT) the dissipation of the PMF by UCP1-mediated proton leakage, decreases the ratio of [ATP]/[ADP] and the metabolic transformation of substrates required for the electron transport is released as heat [9]. The heat generated in BAT results in non-shivering thermogenesis in neonatal and cold-acclimatized mammals [9].

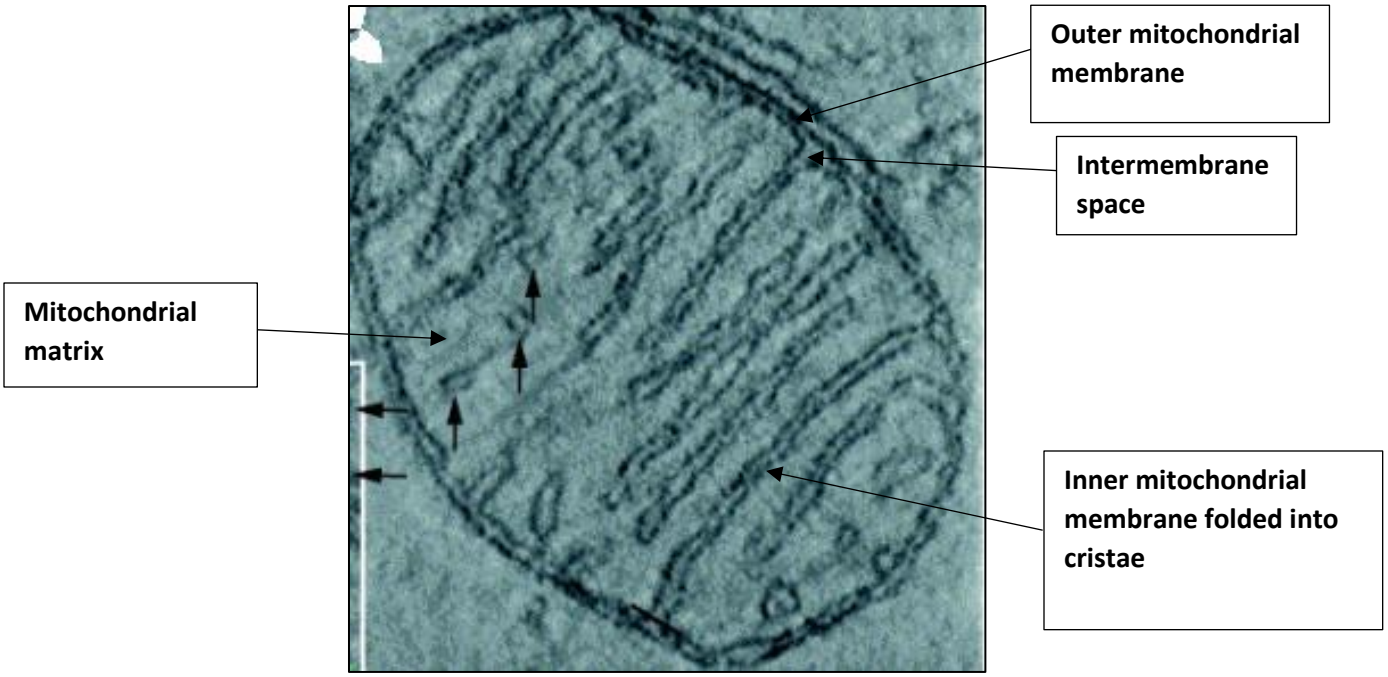

Figure 1: An Electronmicrograph of the mitochondrion. The long arrows indicate the outer mitochondrial membrane, intermembrane space, inner mitochondrial membrane, and the mitochondrial membrane. The mitochondrion was isolated from chick cerebellum. Reprinted by permission from Elseivier (Frey, T., Renken, C., and Perkins, G. (2002). Insight into mitochondrial structure and function from electron tomography. Biochimica et Biophysica Acta (BBA) - Bioenergetics, 1555(1), 196–203), copyright 2002.

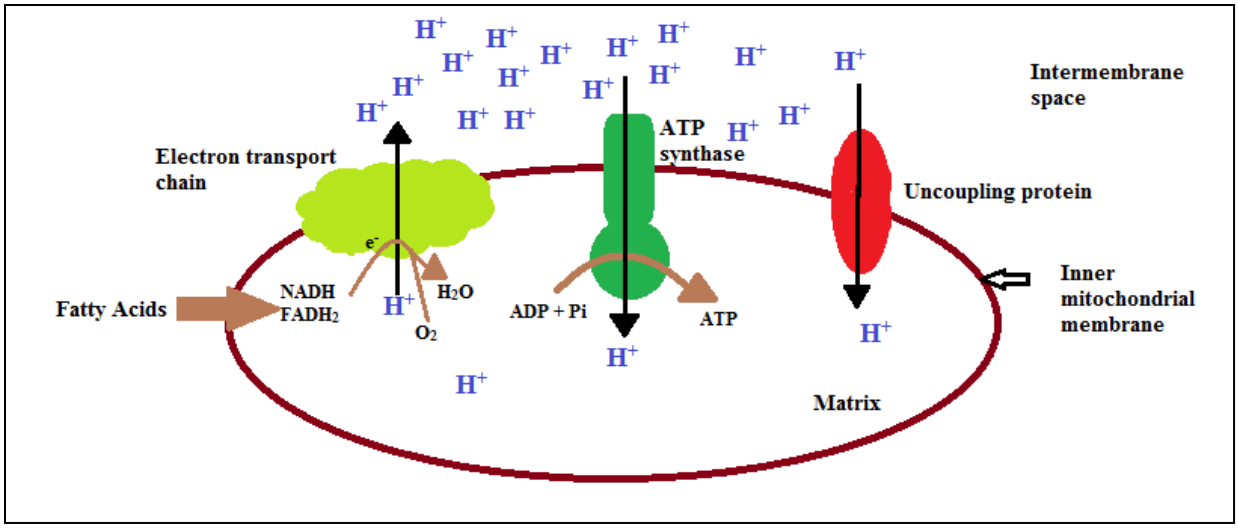

Figure 2: Process of ATP synthesis and UCP-mediated proton leakage in the mitochondria. NADH and $FADH_2$ transfer their electrons to the protein complexes in the electron transport chain. As the electrons move through the complexes, protons are pumped from the matrix into the intermembrane space which forms a proton motive force across the inner mitochondrial membrane. The proton motive force drives ATP production in ATP synthase, however, its dissipation by UCP decreases ATP synthesis. Stephanie Uwumarenogie created this image with the Microsoft paint.

1.2. Uncoupling Proteins

Research in the late 1970's established BAT as the major source of non-shivering thermogenesis in hibernating and infant mammals [10, 11]. Experimental evidence showed that a key contributor to heat production in BAT was the uncoupling of cellular respiration from ATP synthesis in the mitochondria [12]. However, it wasn't until 1978 that photo-affinity labelling experiments showed that rat isolated mitochondria had increased proton leakage in the presence of free FAs [13]. In turn, decreased proton leakage was observed in the presence of purine di- and tri-phosphate nucleotides [13]. It was then discovered that an IMM protein was responsible for this phenomena and this protein was called UCP [11, 14]. UCP activity in BAT is sensitive to stimuli from cold exposure and diet. In BAT, cold stress and over feeding triggers β-adrenergic stimulation of lipolysis. This increases the free fatty acid concentration in BAT and relieves UCP

of nucleotide inhibition. In turn, UCP-mediated proton leakage is activated and results in less ATP production while the metabolic transformation of substrates required for ETC is released as heat [15, 16]. As a result, the role of this UCP was extended to the control of body weight and obesity [17].

Upon discovering other UCP homologues in 1997, the UCP found in BAT was renamed UCP1 [18]. UCP2 has 59% sequence identity to UCP1 and is found in various tissues including pancreatic β-cells, liver, kidney and cerebellum [18]. UCP2 is proposed to influence glucose stimulated insulin secretion in pancreatic β-cells and regulate reactive oxygen species (ROS) production in the mitochondria [19, 20]. UCP3 has 57% sequence identity to UCP1 and is predominantly found in skeletal and heart muscle [21]. UCP3 is hypothesized to regulate ROS production, FA transport, and glucose metabolism in skeletal muscle [21, 22]. The most recently discovered homologues, UCP4 and UCP5, are found in the central nervous system with 30% and 34% sequence identity to UCP1 respectively [16, 23, 24]. Their physiological roles include regulation of neuronal calcium secretion and reduction of reactive oxygen species [16, 23, 24].

1.3. Structure of Uncoupling Proteins

Although five UCP homologues have been identified, their detailed structure at high resolution is yet to be elucidated. This is because membrane proteins need a membrane environment to maintain their structure and function [25]. *In vitro* studies of membrane proteins require disruption of the membrane microenvironment around the proteins. This process makes it tedious to appropriate samples to perform high-resolution x-ray crystallization or NMR studies [25]. Despite these limitations, the structure of UCPs is proposed to be similar to a member of the mitochondria anion carrier family (MCF) protein, ADP/ATP carrier protein (AAC) (Figure 3A) with which it has ~23% sequence identity [16]. UCPs and AAC share a

common tripartite structure that consists of three pseudo-repeat domains. Each domain contains two transmembrane (TM) α-helices that are joined by loops oriented towards the mitochondrial matrix [16]. Similar to the hypothesized structure, the NMR resolved structure of UCP2 has six TM helices that spans the IMM with the N- and C- terminus located in the IMS (Figure 3B) [26]. However, structural differences exist between AAC and UCP2 including: the helix near the C-terminus of UCP2, the densely packed helices in AAC, and the more open matrix oriented helices in UCP2 (Figure 3A and 3B) [26].

Sequence alignment analysis found a common MCF motif in UCPs and AAC: Px[D/E]xx[R/K] on TM helices 1, 3, 5, and [F/Y][D/E]xx[R/K] located on TM helices 2, 4, and 6 [27]. Apparently, the prolines in the motif form a kink in the odd helices for substrate binding while the charged residues form a salt bridge network that mediates substrate transport through the proteins [27].

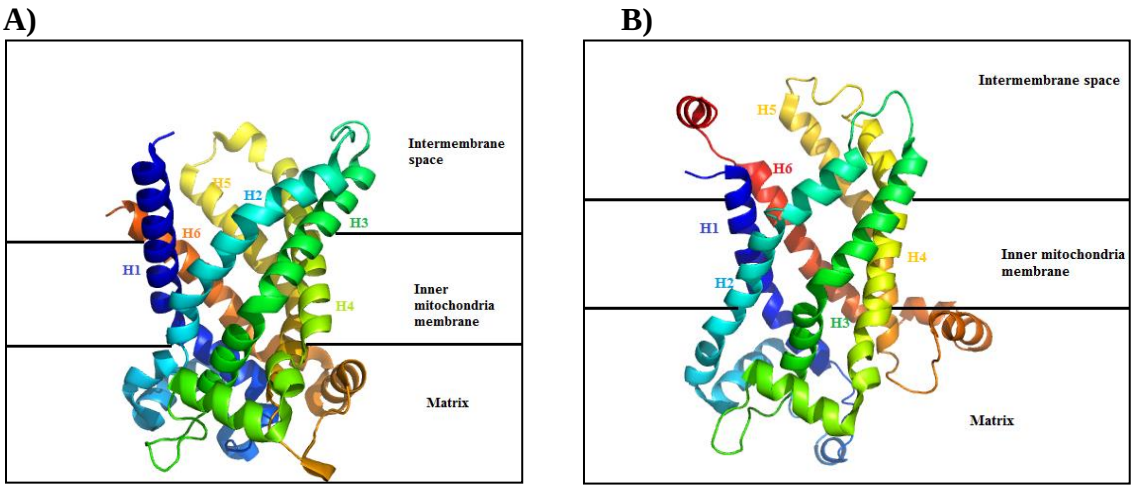

Figure 3: Structural similarity between ADP/ATP carrier protein and UCP2.
ADP/ATP structure (A) was determined with x-ray crystallography [29] while the UCP2 structure (B) was resolved with NMR fragment searching [26]. Lateral view of both structures show six α-helices numbered H1-H6 that span the inner mitochondrial membrane are connected by loops located in the matrix. The structures were viewed in PyMOL [94] using accession numbers 2C3E and 2LCK1 from protein data bank respectively.

1.4. Uncoupling Protein 2

UCP2 is a 33kDa protein that has the largest tissue distribution amongst all UCPs. High levels of UCP2 mRNA are detected in many tissues including heart, skeletal, BAT, kidney, liver, and the central nervous system. However, the protein has only been found in pancreatic β-cells, spleen, and hypothalamus, which imply a tight regulation of UCP2 at the translational level [9, 18].

Since UCP2 has a high sequence identity to UCP1, researchers initially assumed the main role of UCP2 was thermogenesis. But experimental evidence showed that mice with their UCP2 knocked out was insensitive to cold and diet induced thermogenesis [29]. This implied that thermogenesis was not the main function for UCP2 [29].

Further research associated the UCP2 activity to the regulation of ROS production. In the mitochondria, 70–80% of ROS are produced as superoxide radical anions ($O_2^{\cdot -}$) by Complex III in the ETC [30]. These superoxide anions are highly reactive and can cause oxidative stress. Oxidative stress is linked to aging and neurodegenerative diseases like Alzheimer's and Parkinson's [9]. Although the mitochondria have a unique set of antioxidant enzymes that removes superoxide radicals, UCP2 mediated proton leakage could also decrease superoxide anion production in the mitochondria. A high membrane potential results in the formation of superoxide anion at complexes I and III [30]. Therefore, the dissipation of the electrochemical gradient by UCP2 decreases the membrane potential thereby reducing ROS production [9, 30].

In addition, UCP2 activity is also linked to the immune response in macrophages. One study showed that mice macrophages with knocked out UCP2 survived longer when infected with *Toxoplasma gondii* parasite compared to mice with functional UCP2 [31, 32]. UCP2 is also

proposed to play a role in obesity, cancer and regulation of insulin secretion in β cells, obesity and cancer [20].

1.5. Ion Transport and Nucleotide Inhibition in UCPs.

Despite the proposed physiological roles of UCPs above, the mechanism of proton leakage by UCPs is still debated. So far, three main mechanisms of proton transport have been proposed for UCPs: the fatty acid (FA) cycling model [33], cofactor model [34], and shuttling model [35]. The FA cycling model states that UCPs transport FA anions from the matrix into the intermembrane space, where it accepts a proton and flip-flops across the IMM into the matrix. Once in the matrix, the FAs release the protons and the FA anion is transported back to the intermembrane space via UCP to repeat the cycle (Figure 4A) [33]. In contrast, the cofactor model states that FA bind to UCPs and uses its carboxylate anion to transport protons from the intermembrane space to UCPs ionizable amino acid residues, and finally into the matrix (Figure 4B) [34]. Recently, a FA shuttling model was proposed in which FA anions bind to UCP via their hydrophobic chain. UCP transports the FA anion towards the intermembrane space to get protonated. After which, UCP simultaneously transports the FA and proton towards the matrix. However, the FA remains bound to the protein after releasing the proton, and UCP transport's the FA anion for another translocation cycle (Figure 3C) [35]. Unfortunately, multiple experiments have refuted each of the competing models, making it difficult to deduce a specific mode of transport for UCPs.

Though it is generally accepted that FAs activate UCP proton transport, current research has indicated that ROS also activate UCP uncoupling activity. It is proposed that ROS oxidize a specific cysteine thiol residue and results in FA displacement of nucleotides and activation of

FA-mediated uncoupling in UCPs. Furthermore, mutation of this cysteine residue desensitized UCP1 to purine inhibition [36].

In vitro studies show that UCPs also transport small anions such as chloride (Cl^-), nitrate (NO_3^-), and alkylsulfonates ($R\text{-}SO_3^-$). Mutagenic studies revealed amino acids in TM 2 of UCP1 can be responsible for Cl^- transport [39]. In addition, FAs are suggested to competitively inhibit UCP Cl^- transport [37-39].

It is also known that UCPs are inhibited by purine di- and tri-phosphate nucleotides (ATP, ADP, GTP, GDP). Site directed mutagenesis identified arginine and glutamate residues in UCP1 that are involved in binding purine nucleotides [16]. The arginine residues bind the sugar moiety and phosphate groups of the nucleotide while glutamate stabilizes these interactions [16]. Although, there is ample information to support UCPs proton transport, anion transport and nucleotide inhibition, more research must be performed to establish the mechanism of these processes and their potential correlation to each other [9, 16].

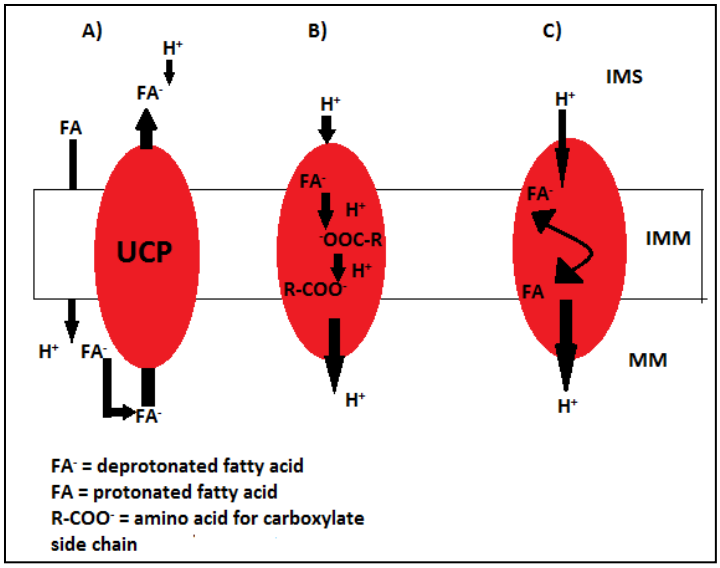

Figure 4: Proposed mechanisms for fatty acid mediated proton transport by UCP. **A)** Cycling model: FA anions are transported by UCPs into the intermembrane space (IMS). There, the FA anion becomes protonated, flip flops across the inner mitochondrial membrane (IMM) and releases the protons into the mitochondrial matrix (MM). **B)** Cofactor model: FA anions bind to specific sites on UCP and accepts protons from the IMS. This proton is buffered through UCP via its ionisable side chains into the MM. **C)** Shuttling model: FA anion binds to UCP and is translocated towards the IMS to accepts a proton. The UCP then translocates the protonated FA towards the MM where the proton is released but the FA remains bound to the protein**.** Stephanie Uwumarenogie created this image with the Microsoft paint application.

1.6. Conserved Motifs in Members of Mitochondrial Carrier Family

Resolving the x-ray crystal structure of AAC led researchers to confirm motifs in the protein that are also conserved amongst the MCF. Sequence analysis identified a highly conserved cytoplasmic and matrix network motif in AAC and some MCF proteins including UCPs [40]. The cytoplasmic motif [F/Y][D/E]xx[R/K] (on even numbered helices) is positioned towards the intermembrane space while the matrix motif PX[D/E]Xxx[R/K] (on odd numbered helices) is located towards the matrix side of the membrane [40 - 42]. Mutating the positively and negatively charged residues to uncharged amino acids in the matrix motif of yeast AAC revealed charged pair interactions between amino acid residues in the matrix network [40]. Furthermore, mutating the charged amino acid residues in the cytoplasmic network of

oxoglutarate transporter (member of MCF) to cysteine showed decreased transport rate up to 15% compared to wild type [43]. These studies suggested that the charged residues in both motifs might influence substrate binding and the mechanism of transport in AAC and other members of the MCF [42, 43].

Symmetry analysis and the measurement of interaction energies between amino acids in both networks of AAC and UCPs, revealed that charged amino acids in the cytoplasmic network form salt bridges between TM 2, 4, and 6 while the charged amino acids in the matrix network form salt bridges between TM 1, 3, and 5 (Figure 5) (Figure A1) [42, 44]. In proteins, salt bridge interactions are defined as non-covalent interactions between oppositely charged amino acids that play vital roles in protein folding, substrate binding and transport [45]. In 2006, Robinson and Kunji [42] proposed a mechanism of substrate translocation that involved the formation and disruption of the cytoplasmic and matrix salt bridge networks in MCF proteins. The proposed mechanism stated that when a substrate was bound to the central cavity of the MCF protein, a conformational change was induced in the protein. This conformational change enabled the charged residues in the cytoplasmic network to form a salt bridge that closed the protein toward the intermembrane space. Concurrently, the matrix salt bridge was disrupted so that the substrate was released into the matrix. Meanwhile, when a substrate was exported out of the matrix, the matrix salt bridge network was formed while the cytoplasmic salt bridge network was disrupted [42]. On this basis, the charged residues in the cytoplasmic and matrix salt bridge network could play an important role in the ion transport mechanism of MCF proteins including UCPs.

In the cytoplasmic network of UCP2, K104 (TM2) and K295 (TM6) form a salt bridge interaction with D198 (TM4) and D101 (TM2) respectively (Figure 6A). While in the matrix network K38 (TM1), K141 (TM3), and K239 (TM5) form a salt bridge interaction with D236

(TM5), D35 (TM1), and D138 (TM3) respectively (Figure 6B) [42]. However, the effect that the charged residues in both networks may have on ion transport mechanism of UCP2 has not been proven experimentally. Therefore, in this study, the role that positively charged lysine residues in the matrix salt bridge network have on the ion transport activity of UCP2 was investigated.

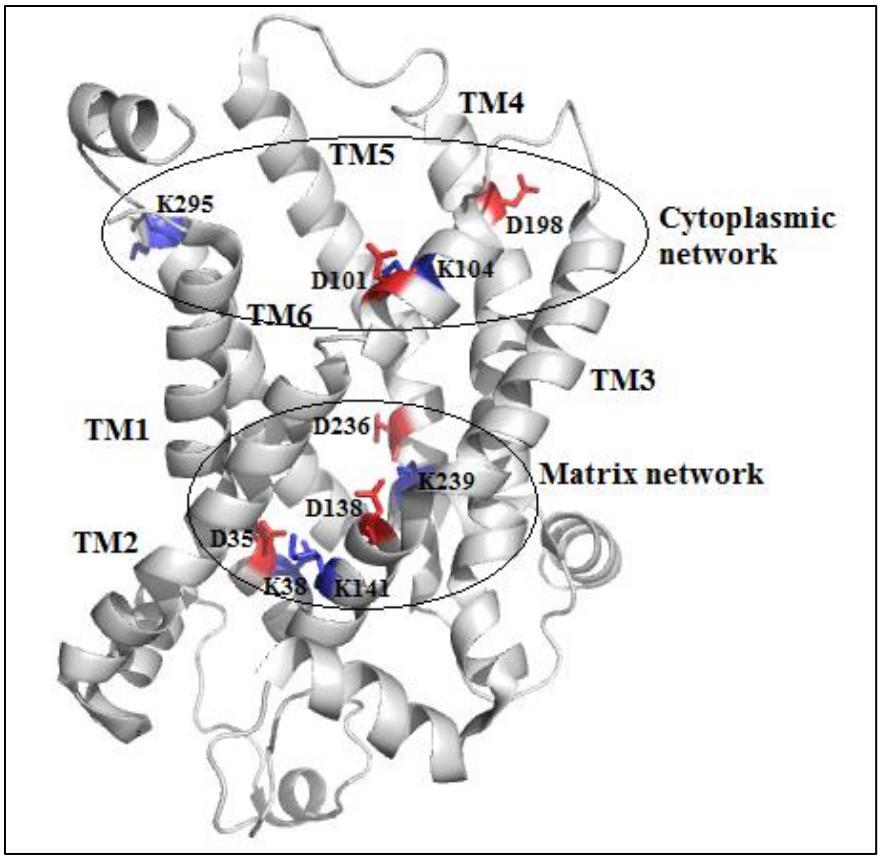

Figure 5: Side view of the charged amino acids in the cytoplasmic and matrix network of UCP2. Positively charged lysine (K) and negatively charged aspartate (D) amino acids in both networks are highlighted in blue and red respectively. The transmembrane helices are numbered 1 – 6. Charged residues in the cytoplasmic network are highlighted by the big oval while the small oval highlights the cluster of charged residues in the matrix network. The sizes of the oval differ because the structure was resolved with GDP bound which locked the protein in a state that was open to the intermembrane space and closed toward the mitochondrial matrix. The NMR resolved structure of UCP2 structure was viewed in PyMOL [94] using accession number 2LCK1 from the protein data bank.

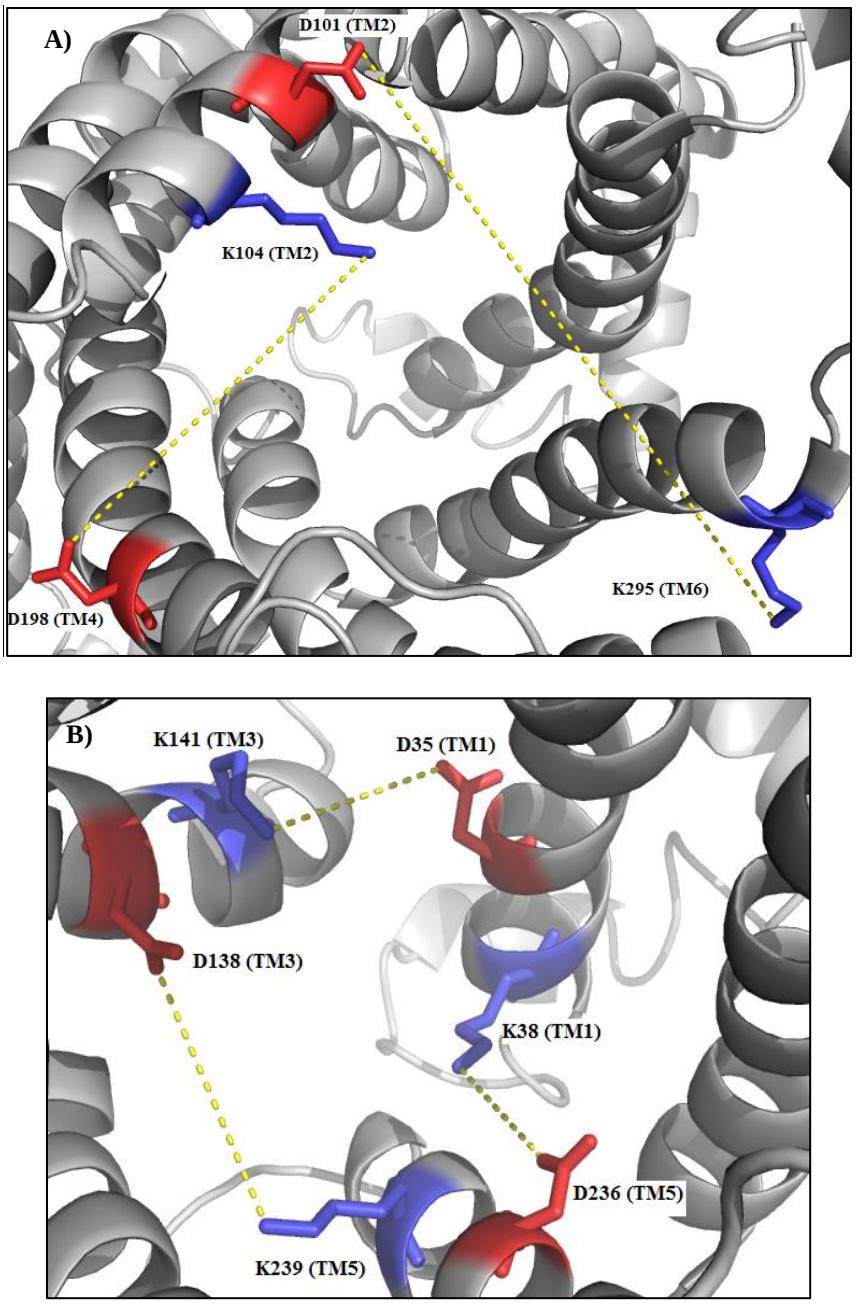

Figure 6: Proposed cytoplasmic and matrix salt bridge interactions in UCP2. Positively charged lysines are highlighted in blue while negatively charged aspartate amino acids are highlighted in red. The dashed line represents the proposed salt bridge interaction between oppositely charged amino acids in the networks. **A)** Salt bridge interactions between lysine and aspartate residues in TM 2, 4 and 6 in the cytoplasmic network; **B)** Salt bridge interactions between lysine and aspartate residues in TM 1, 3 and 5 in the matrix network. The amino acids in the networks were viewed from the cytosolic side (top view) of the NMR resolved structure of UCP2 protein. The UCP2 structure was viewed in PyMOL [94] using accession number 2LCK1 from the protein data bank.

1.7. Research Objectives

The overall objective of this research project was to further understand the mechanism of ion transport in UCP2. To achieve this objective, point mutations were introduced into the matrix network of UCP2 cDNA to specifically probe the role of lysine residues in this network on the ion transport mechanism of the protein. The lysine residues in the matrix network were replaced with glutamine to eliminate the positive charge required for a salt bridge interaction with the negatively charged aspartate amino acid residues in the network. Past studies showed that the proton transport activity of UCPs are activated by free FAs and inhibited by purine di- and tri-phosphate nucleotides [7, 46]. Therefore, the effect of the mutations on the proton transport rate of UCP2 in the presence and absence of purine nucleotides could determine the role of lysine residues in the matrix salt bridge network on the proton transport mechanism and possibly nucleotide binding activity of UCP2.

Due to the proposed role of the matrix salt bridge network on substrate translocation in MCF proteins [42], it was expected that the mutations would destabilize the matrix salt bridge network and diminish the proton transport activity of UCP2. Furthermore, since the amino acid residues involved in nucleotide binding are located near the matrix salt bridge network of UCP2 (Figure 7), these mutations could also alter the nucleotide binding site and either enhance or decrease nucleotide inhibition of FA-mediated proton transport in UCP2.

To achieve the above objective, the following steps were successfully performed: Firstly, the lysine residues at positions 38, 141, and 239 in the matrix network of UCP2 were changed to glutamine using site directed mutagenesis. More specifically, overlap extension polymerase chain reaction (PCR) technique was utilized to introduce three single mutations and a double mutation into the UCP2 cDNA. Secondly, the mutant and wild type UCP2 proteins were

expressed in and further isolated from the inner membranes of *Escherichia coli* (*E.coli*). After which the dominantly monomeric proteins were purified with immobilized metal affinity chromatography (IMAC). Thirdly, far-UV circular dichroism (CD) was used to determine the overall conformation of the mutant and native UCP2 proteins. In the final step, a fluorescence-based assay was used to measure the proton transport activity of UCP2 and its mutants in the presence and absence of ATP. Overall, experimental results from this project could expand our knowledge on the mechanism of ion transport in UCP2 and other UCP homologues.

A detailed explanation of the molecular biology and biophysical techniques used in this project are described in subsequent sections.

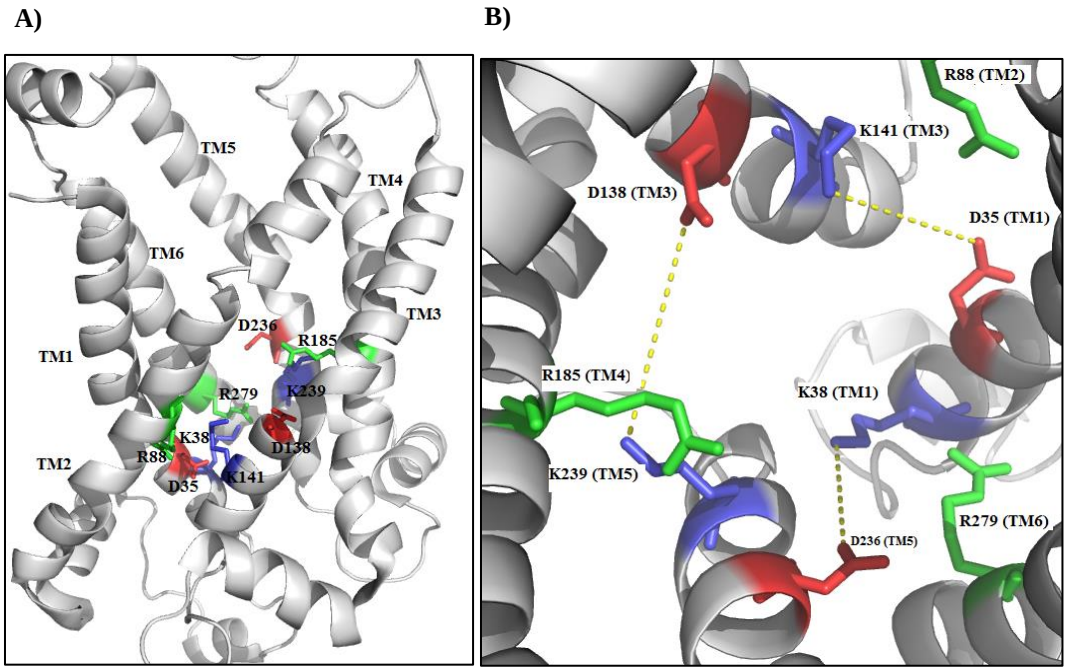

Figure 7: Arginine residues involved in nucleotide binding in UCP2. Arginine residues (R88, R185, and R279) are highlighted in green, while the blue and red colours highlight the lysine and aspartate residues in the UCP2 matrix network. The dashed line represents the proposed salt bridge interaction between oppositely charged amino acids in the matrix network. **A)** Side view of the nucleotide binding arginine residues and the matrix network. **B)** Cytosolic view (top view) of the arginine residues and matrix salt bridge network. The UCP2 structure was viewed in PyMOL [94] using accession number 2LCK1 from the protein data bank.

CHAPTER 2: MOLECULAR BIOLOGY AND BIOPHYSICAL TECHNIQUES USED TO STUDY THE STRUCTURE AND FUNCTION OF MEMBRANE PROTEINS

2.1. Overlap Extension Polymerase Chain Reaction (PCR)

To investigate the role that positively charged residues in the matrix network had on the ion transport activity of UCP2, the lysine residues at positions 38, 141, and 239 were changed to glutamine. Glutamine was chosen to replace lysine because they are relatively similar in size and structure. However, the uncharged nature of glutamine ensured the salt bridge interaction between lysine and aspartate in the matrix network was disrupted so that the effect of the mutations on transport activity of UCP2 could be measured.

In total, three single mutants and one double mutant UCP2 cDNAs encoded the proteins: K38Q, K141Q, K239Q and K38Q/K239Q. The mutations were inserted into the cDNA UCP2 cDNA using overlap extension PCR. In this technique, mutations were introduced into the UCP2 cDNA with mutagenic primers in two separate PCR reactions [47]. In a third PCR reaction, the DNA fragments from the reactions were made single stranded and the overlapping region enabled the products from each reaction to hybridise and form the final nucleotide sequence with the targeted mutation. [47]

More specifically, the first PCR reaction required a sense flanking primer (A) that hybridized to the end of the UCP2 cDNA, and an antisense mutagenic primer (B) that contained the mismatched bases and hybridized to the mutation site [47]. Attached to the end of primer A, was an NcoI restriction site that enabled the insertion of the mutated cDNA into an expression vector, as well as a polyhistidine-tag (His-tag) that allowed the purification of the expressed

protein with IMAC. Similarly, the second PCR reaction involved an antisense flanking primer (D) that hybridized and added a HindIII restriction site to the other end of the cDNA, as well as a sense mutagenic primer (C) which hybridized to the site of the cDNA to be altered [47, 48]. In the final PCR reaction, the PCR products AB and CD from the first and second reactions were denatured and annealed which enabled overlapping strands to hybridize. The overlapping hybrid strands containing a 3'-hydroxyl group, were extended by DNA polymerase to form the cDNA product with the appropriate mutation. The mutated cDNA was further amplified in several PCR cycles with the flanking primers (A and B) (Figure 8) [47, 48]. Each mutated cDNA product was cloned into an expression vector for transformation into bacterial cells.

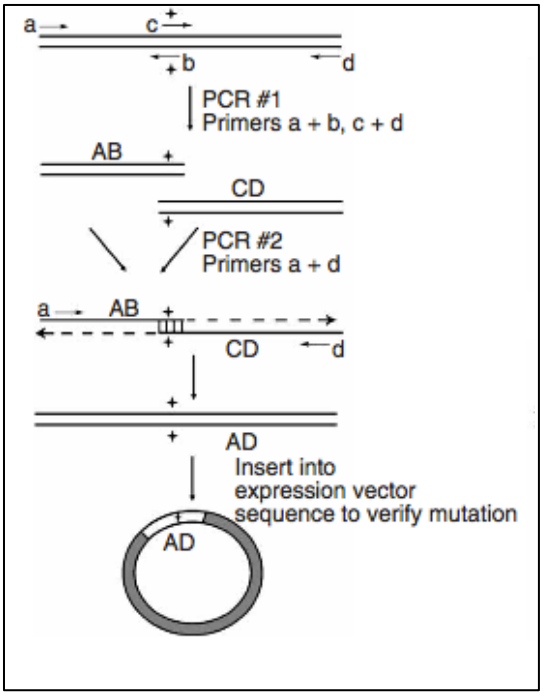

Figure 8: An illustration for the process of overlap extension polymerase chain reaction. Primers B and C represent the mutagenic primers while primers A and D are the flanking primers. Retrieved with permission from Nature [48], copyright 2007.

2.2. Cloning, Protein Expression, and Purification

Once the UCP2 mutant cDNAs were produced, the cDNA products were cloned into a pET26b(+) vector. The pET26b(+) vector was chosen because it encoded the antibiotic resistance gene for kanamycin and also a pelB signal peptide. The signal peptide targeted the expressed mutant proteins towards the periplasmic space as a means to allow the proteins fold in the bacteria inner membrane [49, 50]. To clone the cDNA into the pET26b(+) vector, both components were digested with NcoI and HINDIII restriction enzymes to create sticky ends. The sticky ends allowed the ligation of theDNA into pET26b(+) using T4 DNA ligase enzyme and formed a recombinant vector (Figure 9) [51]. Next, the recombinant vector was transformed into *E.coli* cells through heat shock. During heat shock, chemically competent bacteria cells were exposed to cold and hot temperatures to briefly disrupt the bacteria membrane to take up the recombinant vector (Figure 9) [51]. After transformation, the recombinant proteins were expressed via auto-induction, where lactose and glycerol served as carbon sources after glucose was consumed by the bacterial cell [52]. The expressed proteins were isolated from bacteria membranes and purified with IMAC.

In the next step, the protein's purity and relative molecular mass was assessed with a sodium dodecyl sulfate polyacrylamide gel electrophoresis (SDS-PAGE). SDS-PAGE is a method whereby proteins are denatured and separated by size [53]. Protein separation is achieved by the difference in their migration rates through a gel matrix that is composed of crosslinked acrylamide polymers [53]. In this technique, an anionic detergent called SDS linearized the folded state of the protein and gave the polypeptide chain an overall negative charge. Once, the denatured protein was applied onto the SDS gel, an electric current was applied that allowed proteins to move through the gel matrix according to their size [53, 54]. After the size and purity

of each protein were confirmed, the proteins were further identified using a western blot technique [55]. In this method, the proteins resolved on an SDS-PAGE gel were transferred onto a nitrocellulose membrane, and incubated with a polyclonal antiUCP1/2/3 primary antibody that bound to a specific UCP2 sequence on the proteins. After the unbound antibodies were washed off the membrane, the bound antibodies were detected with a secondary antibody linked to an enzyme that cleaved a chemiluminescent agent. The illuminescent product was visualized on an imager and the detected band corresponded to the identified protein [55].

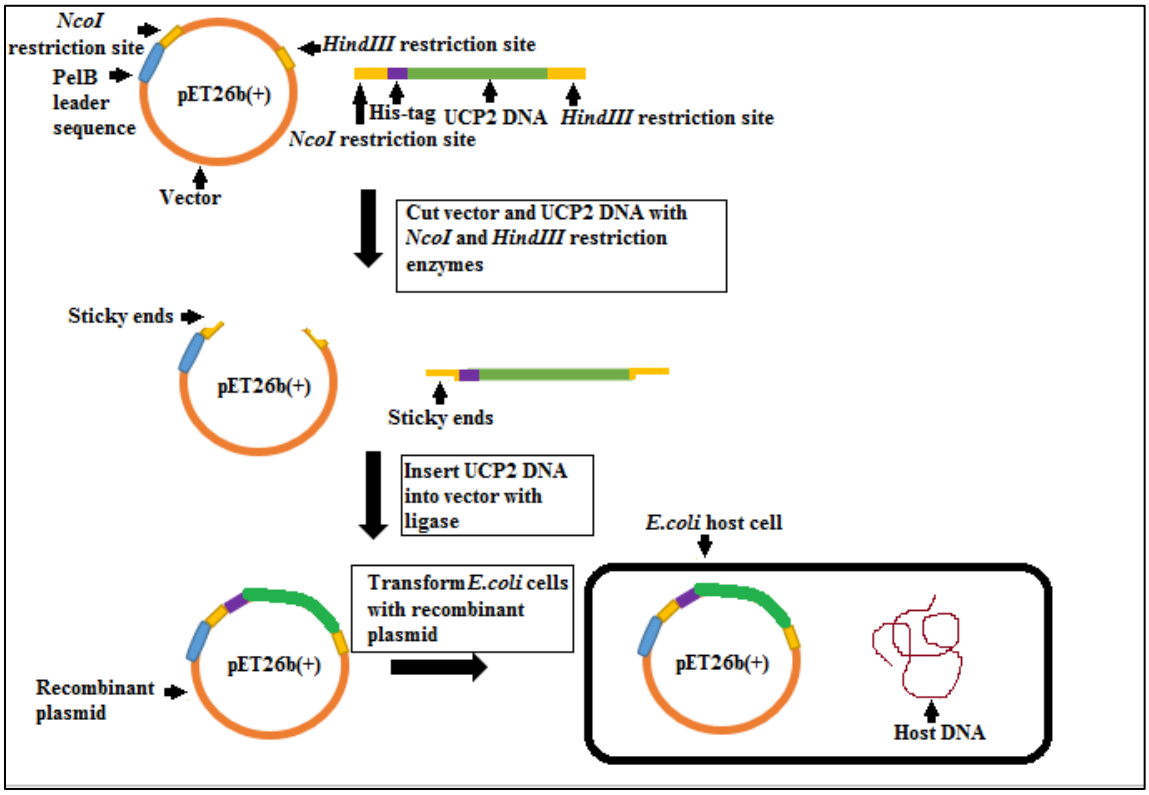

Figure 9: Cloning UCP2 gene into pET26b(+) vector. The UCP2 mutant genes were synthesized with an NcoI and HindIII site for ligation into the pET26b(+) plasmid. The recombinant vector was transformed into *E.coli* cells for protein expression. Stephanie Uwumarenogie created this image on Microsoft paint.

2.3. Reconstitution of Membrane Proteins into Phospholipid vesicles

In vitro studies of integral membrane proteins rely on proper incorporation of these proteins into lipid bilayers to ensure they maintain their native folded state [56]. In reconstitution, membrane proteins are inserted into phospholipid vesicles (liposomes) to mimic the protein's interaction with cellular membranes. Proper reconstitution of membrane proteins into liposomes is essential for their structural and functional studies [56].

Liposomes are composed of one (unilamellar vesicles) or more (multilamellar vesicles) phospholipid bilayers that enclose an aqueous compartment [56]. Liposomes are made when phospholipids that form bilayer structures are dispersed in aqueous solution, and spontaneously associate in aqueous media [56]. This association is favoured because the hydrophobic acyl chains are buried in the hydrophobic center while the hydrophilic head groups interact with the aqueous solvent [56]. In addition, the edges of the phospholipid bilayer are sealed to form vesicles to ensure the acyl chains are not exposed to the aqueous solution [56]. Liposomes can be used to administer drugs, and study the folding and ion transport properties of membrane proteins [56]. Liposomes embedded proteins are known as known as proteoliposomes [56].

Liposomes can be small unilamellar vesicles (SUVs) with diameters of 20 nm – 50 nm. Due to the small size and high curvature, SUVs tend to fuse to form larger vesicles [56, 57]. Meanwhile, large unilamellar vesicles (LUVs) with diameters from 100 nm to 1 μm [56], are desired for most reconstitution studies because of their decreased curvature that implies better stability for ion transport assays across and other biophysical studies [56, 57].

Reconstitution of integral membrane proteins into liposomes can be accomplished through different techniques, including: reverse-phase evaporation, sonication, and detergent-mediated reconstitution [57]. In reverse-phase evaporation, phospholipids, membrane proteins,

and an aqueous buffer are mixed in excess organic solvent. Evaporating the organic solvent from the emulsion results in the formation of proteoliposomes [57, 58]. During sonication, phospholipids and membrane proteins are rehydrated in aqueous buffer. The phospholipid and protein suspension forms multilamellar vesicles (MLVs) with proteins embedded in the bilayers which are ultimately are broken into SUVs with sonic energy [59]. A limitation of both techniques is that the organic solvent in reverse-phase evaporation and high pressure from sonication often denature the membrane proteins [57, 59].

To avoid the above-mentioned complications, detergent-mediated reconstitution was the method used in this project. In this method, a dry phospholipid film is rehydrated in aqueous solvent to form MLVs, followed by solubilisation in detergent to form mixed micelles [57]. The purified membrane protein (already solubilized in a detergent) is then added to the mixed micelle to form a lipid-protein-detergent mixed micelle complex [57]. Detergent is removed with dialysis for detergents with high critical micelle concentration (CMC) or by hydrophobic adsorption onto polystyrene beads. Detergent removal from the lipid-protein-detergent mixtures allows the protein to incorporate into LUVs [57].

Overall, protein reconstitution into liposomes is a vital step for studying the biophysical properties of proteins outside the cell membrane. However, liposome size and homogeneity must also be assessed to ensure results from such studies are accurate and reproducible.

2.4. Analysis of Liposome Size Distribution and Stability with Dynamic Light Scattering

Dynamic light scattering (DLS) is technique often used to study protein aggregation, ligand binding to macromolecules as well as the size and homogeneity of liposomes [60, 61]. DLS measures the size distribution of particles that experience Brownian motion in a liquid [60].

Brownian motion describes the random movement of particles suspended in a medium, due to collisions between the particles and molecules in the medium. As a result, Brownian motion in larger particles is slowed down compared to smaller particles [60]. DLS correlates the intensity of scattered light by particles in Brownian motion to the size of particles in a sample [60].

In DLS technique, a sample is illuminated with a polarized beam of light from a laser source. The incident light is scattered in different directions upon contact with the surface of the particle in the sample [61]. A detector measures the intensity of scattered light by the sample and transferred to a correlator [61]. The correlator compares the level of similarity between two intensities measured at different time points. Furthermore, this comparison is used to determine the rate at which the intensity of scattered light fluctuates over time [61]. Due to Brownian motion, smaller particles fluctuate the scattered light intensity at faster rates compared to larger particles [60, 61]. Furthermore, the size distribution of the sample is can be determined from a Gaussian distribution curve of percent intensity of light scattered versus size of particle. [62]. A narrow width curve indicates a monodisperse sample while a wide width curve shows a polydisperse population of particles in the sample [62].

2.5. Analysis of Protein Secondary Structure with Circular Dichroism Spectroscopy

Circular dichroism (CD) is the difference in the absorption of left- and right-handed circularly polarized light by chiral chromophores [63]. Chirality is either an intrinsic property of chromophores or induced in them when subjected to a chiral environment.

CD spectroscopy is a technique often used to estimate the average secondary structure of proteins [63]. CD spectra of proteins are measured with a spectropolarimeter. A CD spectrometer uses a high-energy xenon light source to radiate circularly polarised light through a

modulator, which splits it into left- and right-handed circularly polarised light. When an optically active molecule preferentially absorbs one form of the polarised light over the other, the detected emitted light is the difference between the two and is shown as ellipticity. The CD spectrum for the molecule is generated as changes in ellipticity (θ) in millidegrees versus changes in wavelength [63].

In the far-UV range (260 – 180 nm) the differential absorption of circularly polarised light by the protein's backbone peptide bonds yields CD spectra. Absorption in this wavelength range is mostly due to $n \rightarrow \pi^*$ or $\pi \rightarrow \pi^*$ transitions [63]. Each protein secondary structure shows a distinct CD spectrum because the peptide bond chromophores are oriented differently. As a result, the bonds absorb at different wavelengths with varied intensities which gives rise to distinct spectra [63]. Thus, far-UV CD can estimate the overall α-helix, β-sheet, or disordered structure of a protein (Figure 10) [63]. In contrast, CD spectrum in the near-UV region (260 – 320 nm) detects the local environment of protein aromatic side chains and disulfide bonds, which provides information on the tertiary structure of the protein [63]. In addition, CD spectroscopy can also monitor changes in a protein's secondary structure at different temperatures, pH or interaction with ligands. Overall, CD spectroscopy offers a fast and reliable way to determine secondary structure of soluble proteins in aqueous solutions as well as membrane proteins in detergent and liposome systems.

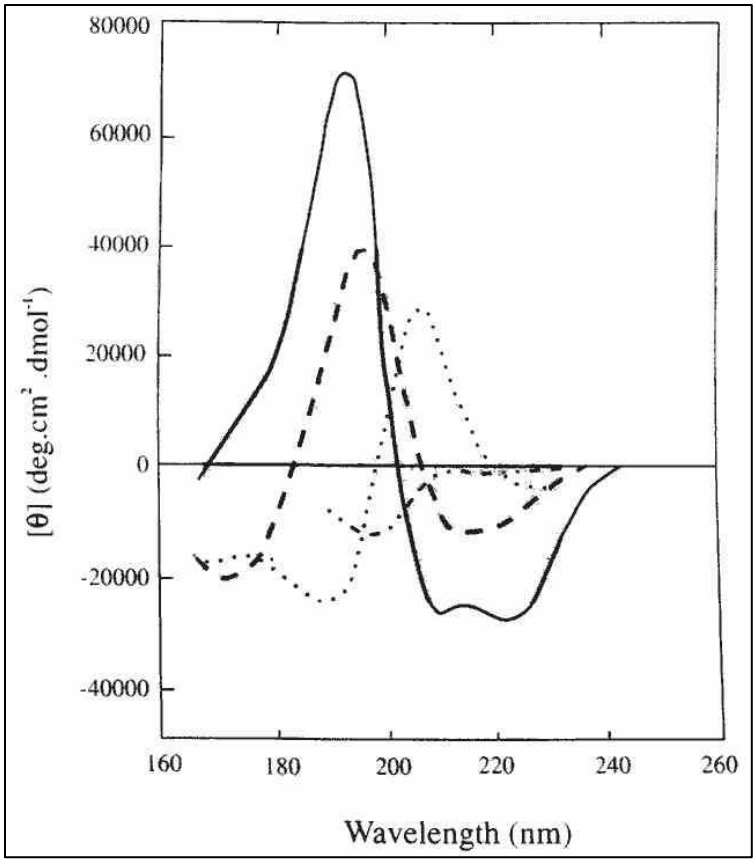

Figure 10: Far-UV CD spectra for protein secondary structures: the solid line represents an α-helix; the dashed line represents an antiparallel β-sheet; the dotted line represents the type I β-turn; and the dots and short dashed line represents a random coil [63].

2.6. Fluorescence Based Ion Transport Measurements across Reconstituted Vesicles

Fluorescence spectroscopy is a technique that is widely used to study the fluorescent properties of biomolecules [64]. Fluorescence is a phenomenon in which light of a particular wavelength is absorbed by electrons in a molecule. Upon light absorption, the electrons are excited from a vibrational energy level in the ground state to a higher vibrational energy level [65]. Some of the energy from the excited electron is lost as they move to the lower vibrational levels of the excited state. Finally, the electrons return to the ground state within 10^{-12}

to 10^{-9} s, and in the process residual energy is emitted as a photon at a longer wavelength [65]. Fluorescence spectroscopy can therefore, analyze the structural, and functional interactions of molecular systems [64, 65].

Proteins have intrinsic fluorophores such as the amino acids: tryptophan, phenylalanine and tyrosine, and sometimes, an extrinsic fluorophore like dansyl-chloride that is covalently attached to the protein [65]. Tryptophan's sensitivity to the polarity of the local environment around it makes it a useful target for fluorescence spectroscopy to study protein dynamics [65]. Thus, a spectral shift in tryptophan's emission may be due to protein folding or unfolding, as well as protein ligand and protein-protein interactions [65].

Fluorescence quenching is a process where the fluorescence intensity of a sample is decreased upon interaction of the fluorophore with a quenching agent [65]. Static and dynamic quenching are considered to be the two main types of fluorescence quenching [65]. In static quenching, a complex is formed at the ground state when the fluorophore and quencher make contact. As a result, when the complex is excited, it returns to the ground state without the emission of light (non-fluorescent) [65]. On the other hand, dynamic quenching is observed when a quencher collides with the fluorophore in its excited state. Upon contact, the energy released by the excited fluorophore is transferred to the quencher and therefore, no light is emitted by the fluorophore when returned to the ground state [65]. Commonly used dynamic quenchers are, oxygen, acrylamide and halogens [65]. With fluorescence quenching the topology of a protein or biological membrane can be probed. This is based on the accessibility of the fluorophore, tagged to a protein or phospholipid, to the quenching agent [65].

Fluorescence quenching technique was also used to develop an assay that can measure proton transport across liposomes [66]. This assay indirectly measured the proton flux with the

fluorescent probe 6-methoxy-N-(3-sulfopropyl) quinolinium (SPQ) [66]. SPQ is a fluorescent dye that is dynamically quenched by halides and anionic forms of zwitterionic buffers like tris(hydroxymethyl)methyl-2-aminoethanesulfonic acid (TES – pKa 7.5) (Figure 11) [66]. At low pH, the TES buffer is predominantly protonated and does not quench SPQ. However, at high pH, TES is mostly in its anionic form and quenches the SPQ signal [66]. SPQ is used to directly detect changes in the concentration of buffers, and indirectly, the change in total acidity (or proton concentration) which is related to proton flux [66]. SPQ quenching by TES, was employed in this study to indirectly measure the rate of proton transport by native and mutant UCP2 proteins.

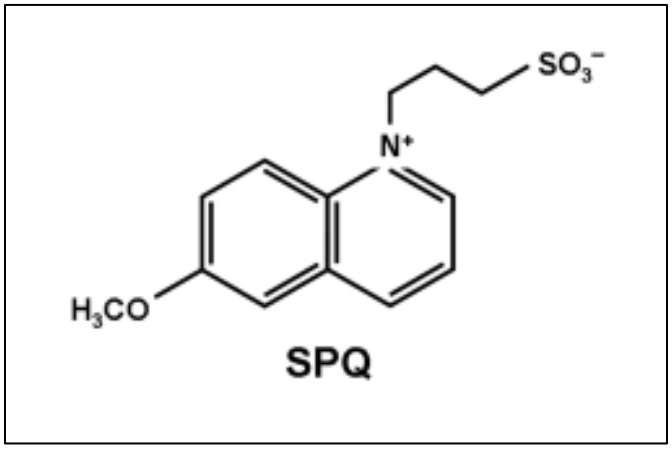

Figure 11: Structure of 6-methoxy-N-(3-sulfopropyl) quinolinium (SPQ). SPQ quenching by TES anion was used to indirectly measure the proton flux by native and mutant UCP2 proteins. This image was retrieved from [67].

CHAPTER 3: MATERIALS, EXPERIMENTAL DESIGN AND METHODS

3.1. Materials

All primers were ordered from Invitrogen™ (Massachusetts, USA). Wizard Plus SV Miniprep DNA Purification System was obtained from Promega (Wisconsin, USA). HotStar HiFidelity DNA polymerase kit was purchased from Qiagen (Germany). E.Z.N.A Gel Extraction Kit was purchased from OMEGA Bio-tek (Georgia, USA). DNA sequencing was performed at The Centre For Applied Genomics (TCAG) Sequencing Facility (Toronto, Canada). 10x CutSmart Buffer, NcoI-HF and HindIII-HF Restriction Enzymes, 10x Ligase buffer with 10mM ATP and T4 DNA Ligase were all purchased from New England BioLabs (NEB) (Massachusetts, USA). All other chemicals used for transformation into *E.coli* cells and protein expression were purchased from Bioshop (Canada). Complete protease inhibitor cocktail tablet EDTA-free was purchased from Roche Applied Science (Indianapolis USA). Lauryldimethylamine-oxide (LDAO) was ordered from Sigma-Aldrich Life Sciences (Missouri, USA), n-octyl-β-D-glucopyranoside (OG) was obtained from Anatrace (California, USA), nickel-nitrilo-triacetic acid-agarose beads (Ni-NTA) were purchased from Thermo Scientific (Massachusetts, USA), tris(hydroxypropyl)phosphine (THP) was ordered from EMD Milipore (Massachusetts, USA), Sephadex G25-300 (Coarse) desalting columns were obtained from GE Healthcare (UK). Rabbit antiUCP1/2/3 and goat anti rabbit antibodies were obtained from Santa Cruz (Dallas, Texas). L-α-Lecithin, composed of at least 60% phosphatidylcholine while the other 40% consisted of phosphatidylethanolamine with trace amounts of cholesterol and triglycerides, was ordered from Sigma-Aldrich (Missouri, USA). 6-Methoxy-N-(3-sulfopropyl)-quinolinium (SPQ) was purchased from Biotium Inc. (California, USA). Sodium palmitate acid

and purine nucleotide (ATP) was obtained from Sigma Aldrich (ON, Canada). SM-2 Biobeads were obtained from Bio-Rad (ON, Canada) while Sephadex G25-300 (Coarse) resins were purchased from GE Healthcare (QC, Canada). Nigericin and valinomycin were purchased from Sigma (ON, Canada) and stored in 100% ethanol at -20^{o}C.

3.2. Experimental Design and Methods

3.2.1. Site Directed Mutagenesis by Overlap Extension PCR

The first phase of this project was to introduce point mutations into the UCP2 cDNA and clone the mutated cDNA's into a pET26b(+) vector with overlap extension PCR . Three single mutant cDNAs encoded the proteins: K38Q, K141Q, and K239Q, and a double mutant cDNA encoded the protein: K38Q/K239Q. The wild type N-terminally, His-tagged UCP2 cDNA that was used as a template for all mutations was cloned into a pET26b(+) vector with its endogenous NcoI knocked out, as described previously [68]. In overlap extension PCR, two separate rounds of PCR that consist of the template, a flanking primer and a mutagenic primer, created two cDNA fragments with overlapping ends. In a third PCR reaction, the products from both reactions served as a template for the flanking primers to amplify the cDNA with the desired mutation [47].

More specifically, the recombinant vector (pet26b(+):UCP2) that contained the native UCP2 cDNA was isolated from DH5α *E.coli* cells. The DH5α cells were grown in 10 mL LB broth that contained 50 μg/mL kanamycin (kan) at 37 ^{o}C, 240 rpm, for 18 h in a shaking incubator. The pet26b(+) vector with the wild type UCP2 cDNA, was extracted from DH5α cells with a Wizard Plus SV Miniprep DNA Purification System as described in the protocol in [69]. Upon which, the isolated recombinant vector was used as a template for the initial two rounds of overlap extension PCR reactions. For the first PCR reaction, an antisense mutagenic

primer, as well as a sense flanking primer that had an NcoI restriction site attached at the 5' end, were incubated in a thermocycler under specific conditions to produce the first overlapping cDNA fragment. Similarly, a second PCR reaction that involved the sense mutagenic primer, and an antisense flanking primer with a HindIII restriction site attached to the 3' end, were used to prepare the second cDNA fragment. The resulting cDNA products from both PCR reactions were run on a 1% agarose gel, at 120V for 1hr, and visualized on a UV transilluminator to confirm the cDNA's with the required length of nucleotide sequence were produced. Next, the PCR products were purified from the gel with an E.Z.N.A Gel Extraction Kit [70]. In the final PCR reaction, the PCR products from both reactions hybridized at the overlapping segments, which are extended by DNA polymerase and further amplified by flanking primers to produce the full-length cDNA with the required mutation.

To create the double mutant cDNA, overlap extension PCR along with the appropriate mutagenic primers was used to generate a full-length cDNA with the first mutation. This cDNA served as the template for another overlap extension PCR that introduced the second mutation into the cDNA.

All PCR reactions were performed with a HotStar HiFidelity DNA polymerase kit (Qiagen) and were prepared in dome capped PCR tubes [71]. The mutant cDNA's were produced with PCR components and thermocycler conditions listed in Tables 1 and 2. In addition, Table 3 provides the nucleotide sequence for the flanking and mutagenic primers utilized in the PCR reactions.

Table 1: Reaction composition by overlap extension PCR: Volume of the components used in PCR reaction to produce each mutant UCP2 cDNA.

Components	PCR Reaction #1 and #2	PCR Reaction #3
5x HotStar HiFidelity PCR Buffer	10 µL	10 µL
100µM Flanking Primer	0.5 µL	0.5 µL (for each sense and antisense)
100µM Mutagenic Primer	0.5 µL	--------
HotStar HiFidelity DNA Polymerase	1 µL	1 µL
RNase-free Water	3 µL	34 µL
Template DNA (50 ng)	2 µL (isolated pET26-UCP2wt)	2 µL PCR product #1 + 2 µL PCR product #2
Total Volume	50 µL	50µL

Table 2: Thermocycler Conditions for All PCR Reactions: The overlap extension PCR reaction required specific temperatures for the cycling steps to efficiently produce the mutant cDNA's.

Cycling Steps$^{\Delta}$	Temperature	Time
Initial Denaturation	95 ^{o}C	5 minutes
Denaturation	94 ^{o}C	15 seconds
Annealing*	63 ^{o}C	30 seconds
Extension	72 ^{o}C	1 minute
Final Extension	72 ^{o}C	10 minutes
Hold	12 ^{o}C	Infinite

$^{\Delta}$Denaturation, annealing and extension steps were repeated for 35 cycles.

* For K141Q, the annealing temperature for 2nd PCR reaction was 65^{o}C.

Table 3: Flanking and Mutant Primers designed for Site Directed Mutagenesis of UCP2

Primer Type	Primer Name	Primers*
Flanking Primer for UCP2wt and all mutants	Sense primer with NcoI restriction enzyme site	5' GGAGATATACCCATGGGAGGATCGCATCACC 3'
	Antisense primer with HindIII restriction enzyme site	5' CCGCAAGCTTGTCGACGGAGCTCTTAGAAGGG 3'
K38Q Mutagenic primer AAA:CAA	Sense primer	5' CCTCTGGATACTGCTCAAGTCCGGTTACAGATCC 3'
	Antisense primer	5'GGATCTGTAACCGGACTTGAGCAGTATCCAGAGG 3'
K141Q Mutagenic primer AAG:CAG	Sense primer	5' CCACGGATGTGGTACAGGTCCGATTCCAAGC 3'
	Antisense primer	5' GCTTGGAATCGGACCTGTACCACATCCGTGG 3'
K239Q Mutagenic primer AAG:CAG	Sense primer	5'CCCTGTAGACGTGGTCCAGACGAGATACATGAAC 3'
	Antisense primer	5' GTTCATGTATCTCGTCTGGACCACGTCTACAGGG 3'

*The restriction enzyme sites in the flanking primer and the specific nucleotide bases changed in the mutagenic primers are highlighted and underlined.

3.2.2. Ligation of UCP2 Mutant cDNA into pET26b(+) and Transformation into DH5α

Once all mutant cDNA's were prepared, the cDNA's were cloned into a pET26b(+) vector. The mutant cDNA's were run on a 1% agarose gel and subsequently purified with the E.Z.N.A Gel Extraction Kit [57]. After which, an empty pET26b(+) vector was isolated from DH5α cells. The empty pET26b(+) and each mutant cDNA (2 µg of each component) were digested with NcoI-HF and HindIII-HF restriction enzymes. Restriction digest reactions were performed at 37 ^{o}C for 3 h in CutSmart buffer. The double digested products were excised from an agarose gel and purified with the E.Z.NA Gel Extraction Kit [70]. Each mutant cDNA was ligated into a pET26b(+) vector, in a ligation reaction that consisted of 300 ng cDNA, 60 ng

vector, 1 μL T4 DNA ligase enzyme, and 1 μL ligase buffer. These components were incubated in a 16 ^{o}C water bath for 16 h.

The ligated products were transformed into chemically competent DH5α cells through heat shock [72]. This was done by the addition of ~100 ng ligated DNA product to 100 μL DH5α competent cells, followed by incubation on ice for 30 min and heat shock at 42 ^{o}C for 90 s. After heat shock, the cells were allowed to recover on ice for 5 min. Next, the cells were diluted to 900 μL with LB broth after which, the cells were grown for 37 ^{o}C, 240 rpm for 1 h. Thereafter, 100 μL of transformed cells were grown overnight, on kanamycin (50 μg/ml) selective agar plates at 37 ^{o}C for 18 h.

After overnight incubation of the transformed DH5α cells, three positive colonies were obtained from the selective media and grown in 10 mL LB and 50 μg/ml kanamycin at 37 ^{o}C, 240 rpm for 16 h. Upon cell growth, the recombinant vector with the appropriate mutant cDNA was extracted from cell culture via Wizard Plus SV Miniprep DNA Purification System [69]. In order to confirm that the isolated vectors had the cDNA incorporated, 1 μg of the recombinant vector was digested with NcoI-HF and HindIII-HF restriction enzymes at 37 ^{o}C for 3 h. The digested products were run on a 1% agarose gel stained with ethidium bromide, and viewed using a VersaDoc 4000 Gel Imaging System (Bio-Rad). Recombinant vectors were confirmed to contain the mutant cDNA if an ~5 Kilobase (kb) band that corresponds to the size of the vector and ~1.05 kb band for the cDNA was identified on the gel.

Glycerol stocks were prepared for colonies that had the mutant cDNA by inoculating the cells into a 4 mL LB broth with 50 μg/ml kanamycin and grown at 37 ^{o}C for 16 h. Two glycerol stocks were made for each positive colony, with 500 μL of 50% glycerol and 500uL cell culture. The prepared glycerol stocks were stored at -80 ^{o}C.

3.2.3. Confirmation of Mutant cDNA Sequence and Transformation of the Recombinant Vector into BL21-Codon Plus-RIPL cells

Once the mutant cDNA's were successful cloned into the pET26b(+) vector, the next step was to confirm that the prepared mutant cDNA's, had the desired mutation. To accomplish this step, the recombinant vector with the appropriate mutant cDNA was isolated from DH5α cells. Then, 375 ng of each recombinant vector was sent to the Centre for Applied Genomics (TCAG) sequencing facility where each mutant cDNA was confirmed to have the required mutation. After the nucleotide sequence of each mutant cDNA was confirmed, the recombinant vectors were later transformed into chemically competent *BL21-Codon Plus- RIPL cells* (BL21 CD^+) via heat shock [72]. The transformed cells were grown on a kanamycin (50 μg/mL) selective media for 18 h at 37 ^oC. Three positive colonies were selected from each plate and grown in 10 mL LB broth that had 25 μg/ml chloramphenicol (cam), 50 μg/ml kanamycin (kan), and 25 μg/ml streptomycin (strep), at 37 ^oC, 240 rpm for 16 h. Next, the recombinant vector was isolated from BL21 CD^+ cells and double digested with both NcoI-HF and HindIII-HF restriction enzymes to confirm colonies that contained the recombinant vector. Colonies with the vector were stored at 80 ^oC in glycerol stocks.

3.2.4. Overexpression of Native and Mutant UCP2 in Bl21 CD^+ Cells

The second phase of this project was to express the mutant and wild type UCP2 proteins in BL21 CD^+ cells using the auto-induction method [52]. Firstly, under sterile conditions, 20 mL LB broth that contained 25 μg/mL cam, 25 μg/mL strep, and 50 μg/mL kan was inoculated with a glycerol stock of either the wild type or mutant UCP2 constructs. The overnight culture was grown in a shaking incubator at 37 ^oC, 240 rpm for 18 h. The next day, the overnight culture was

used to inoculate an autoclaved ZY media that was prepared with 930 mL water, 10 g of tryptone and 5 g of yeast extract in a 2800 mL Fernbach culture flask. The ZY media was prepared for auto-induction with the addition of: 1 mL of 1M $MgSO_4$, 20 mL of 50X 5052 [25% glycerol (w/v) 2.5% glucose and 10% lactose], 50 mL of 20X NPS [composed of 0.5 M $(NH_4)_2SO_4$, 1 M KH_2PO_4, 1 M Na_2HPO_4)], as well as, 50 μg/mL kan, 25 μg/mL cam and 25 μg/mL strep. Bacteria cells were grown in the auto-induced media with shaking at 22 °C, 250 rpm, for 22 h. The cells were collected by centrifugation at 8000x*g* for 15 min at 4 ^oC (JLA-10.500 rotor, Beckman Coulter) and cell pellets were stored at -20 ^oC.

3.2.5. Protein Extraction from Bacteria Cells and Purification with Immobilized Metal Affinity Chromatography (IMAC).

The mutant and native UCP2 were isolated from bacterial membranes as described previously [68]. Briefly, the cell pellets obtained from a 2L cell culture were resuspended in 20 mL extraction buffer (20mM Tris-HCl pH 8.0, 500mM NaCl), 1 tablet of c0mplete protease inhibitor cocktail tablet EDTA-free, 0.5 mg/mL DNase, and 0.2 mg/mL of lysozyme. The resuspended cells were incubated on a vertical rotator at 4 ^oC for 30 min and afterwards, the cells were lysed at 4 ^oC, 20 kPsi using a Constant Cell Disruption system T2/40/BA/AA (Constant Systems). The lysed cells were centrifuged at 20,000xg for 20 min at 4 ^oC to separate unbroken cells and inclusion bodies (pellets) from the membrane and soluble proteins (supernatant). The supernatant was ultracentrifuged at 76,000 rpm, 4 ^oC, for 1 h in an Optima™ Max ultracentrifuge (Beckman-Coulter) using an MLA80 rotor (Beckman-Coulter). This step separated soluble proteins (supernatant) from bacterial membranes (pellet) [68].

Using a 20 gauge needle attached to a 3 mL syringe, the bacterial membranes were resuspended in binding buffer (20 mM Tris-HCl pH 8.0, 0.5 M NaCl, 1% LDAO, 20 mM

Imidazole and 1 mM THP, pH 8.0). The detergent solubilized membrane was transferred to a 25 mL Erlenmeyer flask and stirred at 4 ^{o}C for 2.5 h. After incubation, the solubilized membrane was centrifuged at 8000xg for 10 min at 4 ^{o}C to separate insoluble particles (pellet) from the membrane fraction (supernatant) [68]. The membrane fraction was then passed through an IMAC column packed with 4 mL Ni-NTA resin that was pre-equilibrated with 40 mL of binding buffer. The membrane fraction was passed through the column three times to maximize binding of the his-tagged proteins to the column. After that, the IMAC column was washed with 20 mL wash buffer (20 mM Tris-HCl pH8.0, 0.5 M NaCl, 1% OG, 30 mM imidazole, and 1 mM THP) to remove loosely bound proteins. The proteins tightly bound to the IMAC column were eluted from the IMAC with 10 mL elution buffer (20 mM Tris-HCl pH 8.0, 0.5 M NaCl, 1% OG), 400mM imidazole 1mM THP) and ten 1 mL fractions were collected [68].

All 400 mM imidazole eluted fractions where pooled and concentrated using Amicon Ultra-15 Centrifugal Filter (Merck Millipore). The centrifugal filter used had a molecular weight (MW) cut off of 10 kDa. The filter was equilibrated with 2 mL of elution buffer by centrifuging in a swinging bucket rotor at 4000xg, 4 ^{o}C for 15 mins. The 10 mL eluted fractions were loaded onto the centrifugal filter and centrifuged at 4000xg, 4 ^{o}C for 11 mins [7]. The samples were concentrated to 3 mL (3x concentrated) and buffer exchanged into desalt buffer (20 mM Tris-HCl pH 8.0, 50 mM NaCl, 1% glycerol and 1% OG), using an Econo-Pac®10DG Desalting Prepacked Column (GE Healthcare). The concentration of proteins in the desalt fractions were either measured with a Bradford assay or a modified Lowry assay, using bovine serum albumin (BSA) as standards [68]. Afterwards, the most concentrated desalted protein fractions were stored at -80 ^{o}C.

3.2.6. Sodium Dodecyl Sulfate Polyacrylamide (SDS PAGE) Gel Electrophoresis of Purified Proteins

SDS-PAGE was used to analyze the purity and identify of purified UCP2 wild type and mutant proteins based on molecular size. Approximately 20 ng of desalted UCP2 proteins, in 1x SDS sample buffer (10% glycerol, 50 mM Tris-HCl pH 6.8, 1% SDS, and 75 mM DTT) was loaded into the wells of the 4% acrylamide stacking SDS-PAGE gel. The gel was run at 105 V for 75 min to separate the proteins in 12% resolving SDS-PAGE gel. After which, the gel was stained with Coomassie Brilliant Blue for 2 h and destained overnight in 45% methanol and 10% acetic acid solution. The protein bands on the destained SDS-PAGE gel were viewed on the VersaDoc 4000 Gel Imaging System.

3.2.7. Optimization of the Purification Procedure for Wild Type and Mutant UCP2 Proteins

SDS-PAGE analyses of the native and mutant proteins identified higher and lower molecular proteins that co-purified with the desired proteins. As a result, an imidazole step gradient was used to improve the purity of the proteins [73]. The proteins were extracted from bacterial membranes using the procedure described in section 3.2.5. However, after the resuspended membrane fraction was loaded onto the IMAC column in binding buffer and washed with 30 mM imidazole buffer, a 4 mL wash buffer that contained 75 mM imidazole was applied to the column. The column was further washed with a 4 mL wash buffer that contained 100 mM imidazole, while the remaining proteins bound to the IMAC column were eluted with 10 mL of 400 mM imidazole containing elution buffer. The collected fractions from the wash and the elution buffers were analyzed on an SDS-PAGE gel. Although protein purity improved

from the previous purification procedure, the amount of proteins in the purest fractions was insufficient for biophysical analysis.

In order to maximize protein purity and yield, the following imidazole concentrations were used to purify wild type and mutant UCP2 proteins: 10 mM imidazole in the binding buffer, 75 mM imidazole in the wash buffer, and 400 mM imidazole in the elution buffer. The most concentrated protein fractions eluted with 400mM imidazole were desalted in 1% OG. This modified purification protocol was used to purify all mutant and native UCP2 proteins because the SDS-PAGE indicated increased protein purity with sufficient concentrations for further in vitro studies.

3.2.8. Western Blot Analysis of Purified Proteins

The isolated native and mutant UCP2 proteins were verified with the Western blot technique. Firstly, all proteins were loaded onto an SDS-PAGE gel and run under conditions described in section 3.2.6. Rather than staining the gel, the proteins separated on the gel were transferred onto a nitrocellulose membrane at 15 V for 120 min, using the semi-dry transfer method [68]. Next, the nitrocellulose membrane was stained with Amido Black to confirm transfer efficiency, followed by blocking the membrane in TBS-T (10 mM Tris-HCl, 150 mM NaCl, 0.05% Tween 20, pH 7.5) buffer, containing 5% skim milk, overnight at 4^{o}C [68]. The nitrocellulose membrane was probed with a primary antibody, rabbit IgG anti-UCP1/2/3 (1:2000 dilution) for 2h on a horizontal shaker. Afterwards, anti-rabbit IgG peroxidase-conjugated antibody (1:20,000 dilution) raised in goat was used as the secondary antibody. Immunodetection was achieved by luminescence with a Western blot HRP (horse radish peroxidase) substrate, and the detected proteins were observed on a Bio-Rad VersaDoc 4000 Imaging System.

3.2.9. Structural Analysis of UCP2 Proteins by CD Spectroscopy.

The third phase of this project was to analyze the overall secondary structure of the purified UCP2 native and mutant proteins with CD spectroscopy. Firstly, the concentration of each purified protein in desalt buffer (20 mM Tris-HCl pH 8.0, 50 mM NaCl, 1% glycerol and 1% OG) were quantified with the modified Lowry assay as described in 4.1.8. Secondly, 300 μL of each protein (concentrations between 5 - 8.3 μM) was transferred into a 0.1 cm path length quartz cuvette and far-UV CD spectroscopic measurements at 25 ^{o}C were performed in an Aviv 215 spectropolarimeter (Aviv Biomedical, Lakewood, NJ). The AVIV CDSD software was used to subtract the CD spectra of the blank buffer from that of the protein, to correct for any background signal caused by buffer components. This software also converted the CD spectra reported in millidegrees to mean molar residue ellipticity (molar ellipticity).

Furthermore, the CDSSTR (CD secondary structure) deconvolution program website estimated the α-helical contents of the proteins from the far-UV CD spectra. This analysis was performed on the Dichroweb website and was based on a set of 48 reference proteins [74, 75].

3.2.10. Reconstitution of UCP2 Proteins into Liposomes

As a means to perform ion flux measurements on UCP2 proteins a detergent-mediated reconstitution method was used to embed the proteins into liposomes [57, 68]. First, 100 mg/mL stock of L-α-lecithin phospholipids was dissolved in 75% chloroform and 25% methanol, and stored in a sealed glass vial at - 40 ^{o}C. Next, 30 mg of the 100 mg/mL lipid stock was transferred into a 25 mL round bottom flask (RBF) and a gentle stream of N_2 gas was used to evaporate the chloroform and dry the lipids as a thin film, along the sides of the flask. The lipids were further dried overnight under a vacuum to remove any residual chloroform and methanol. The dried lipids were rehydrated with 3 mM SPQ in ultrapure water and with gentle shaking to form

MLVs. The RBF was also placed in a bath sonicator and degassed for (10 s), to remove the lipids stuck on the sides of the flask. The MLVs were solubilized with the addition of 75 mg C_8E_4, in a detergent to lipid ratio of 2.5:1 by mass. This mixture was incubated on ice for 20 min to facilitate the formation of mixed lipid-detergent micelles.

For proton transport assays, a protein to lipid weight ratio of ~1:200 was used to maximize the amount of proteins incorporated into the lipid vesicles. Moreover, 3 μM stock proteins desalted in 1.5x internal buffer (IB) (30 mM TES, 80 mM TEA_2SO_4, and 1 mM EDTA, pH 7.2, 1% OG) were added to the mixed micelles. Protein-free liposome (blank liposome) controls were made in parallel for all proton transport measurements.

Once the proteins were added to the mixed micelles, the composition was flushed with argon gas (30 s) to remove any residual oxygen that may oxidize the phospholipids, followed by incubation on a stir plate for 1 h 30 min at 4 ^{o}C. Subsequently, the lipid-detergent-protein mixture (1 mL) was incubated in a 3 mL syringe column that contained 1.5 mL SM-2 Biobeads, for 2 h at 4 ^{o}C. Detergent adsorption onto SM-2 Biobeads led to the formation of proteoliposomes, as well as the blank liposomes. Once the incubation time elapsed, the proteoliposome/blank liposomes were eluted from the columns after centrifuging at 1000 rpm, for 1 min at 4 ^{o}C. Any residual detergent in the proteoliposome/blank liposome samples was removed with a second incubation in 1.5 mL SM-2 Biobeads (1 h, 4 ^{o}C). The resultant proteoliposome was collected by centrifugation as described above. Lastly, 250 μL proteoliposome/blank liposome samples were loaded into a gel filtration column composed of 3 mL coarse grade Sephadex G25-300 gel filtration. The gel filtration columns were pre-equilibrated with 1x IB and the proteoliposome/blank liposome samples were centrifuged at

2000 rpm, 4 ^{o}C for 2 min (JS 13.1 rotor). Finally, DLS technique was used to measure the size and dispersity of the eluted proteoliposomes/blank liposomes.

3.2.11. Size Determination of Liposomes Size by Dynamic Light Scattering (DLS)

Size distribution of the blank liposomes and proteoliposomes were determined with DLS. DLS measurements for each sample were obtained after 40 μL of sample was loaded onto a microplate. The microplate was placed in a DynaPro Plate Reader II (Wyatt Technologies, California, U.S.A) and 10 measurements were taken for each sample at 25 ^{o}C.

3.2.12. Proton Flux Measurement Mediated by UCP2 Proteins

The ability of UCP2 wild type and mutant proteins to transport protons across reconstituted phospholipid vesicles were determined with an SPQ fluorescence quenching assay (Figure 12) [66]. The assay was performed in a 1 cm pathlength quartz fluorescence cuvette and measured with a Cary Eclipse spectrofluorometer (Varian) instrument. The fluorescence signal of the SPQ probe was excited at 347 nm and emitted at 442 nm with a bandwidth slit of 5 nm. During the measurements, the assay components were constantly stirred at 25 ^{o}C.

Proton flux measurements were obtained from an assay that contained 40 μL proteoliposome and 1.96 mL external buffer (EB) (80 mM K_2SO_4, 40 mM K-TES, 1 mM EDTA, pH 7.2) in the cuvette. At 30 s, 100 μM palmitic acid (PA) was added to the cuvette, after which proton flux was initiated at 1 min with the addition of 1 μM valinomycin. For each scan, the kinetics of proton transport was measured for 4 min after adding valinomycin and a minimum of

5 scans were conducted for the proteoliposome and blank liposome samples. Proton flux measurements were obtained for blank liposomes to measure non-specific proton leakage.

Once the proton transport measurements were completed, the data was calibrated for the SPQ fluorescence signal. This calibration was achieved with the addition of 40μL proteoliposomes to 1.96mL 1x IB in a cuvette [7, 68]. After mixing for 20 s, 2 μL of 1 mM Nigericin (a K^+/H^+ antiporter) was added, which caused a decrease in the SPQ fluorescence signal. At 45 s, and every 15 s afterwards, 2 μL of 2 M KOH was added to the mixture. The calibrated fluorescence signal was fitted to the modified Stern-Volmer equation below:

$$\frac{F_0}{F} = K_q[H^+] + 1 \text{ (Equation 1)}$$

Where F_0 is the initial fluorescence signal before the addition of KOH, F is the fluorescence in the presence of KOH, K_q is the Stern-Volmer constant, and $[H^+]$ is the change of proton concentration in the media [7, 66, 68]. The value of K_q was calculated from the fitted data, and subsequently used to convert the measured fluorescence kinetics into proton efflux using equation 2:

$$[H^+] = \frac{F_0 - F}{F} \times \frac{1}{K_q}[H^+] + \text{ (Equation 2)}$$

The internal volume of the proteoliposome was determined with the standard addition method to calculate the [SPQ] dye trapped inside the vesicles and comparing it to the original [SPQ] used to prepare the proteoliposomes [7, 68]. In brief, 40 μL proteoliposome was added to 1.96 mL of ultrapure water, and at 20 s, 5 μL of 0.25% (w/v) C_8E_4 was added to solubilize the proteoliposome, upon which an increased fluorescence signal was observed. At 45s, 2.5 μL of 100 μM SPQ was added every 15 s for a total time of 2min. A plot of fluorescence signal vs

$[SPQ]_{added}$, was used to derive the [SPQ] inside the vesicles. Dividing the $[SPQ]_{proteoliposome}$ by the original SPQ $[SPQ]_0$ (i.e. 3mM) yielded the internal volume of the proteoliposome.

$$V(\mu L) = \frac{[SPQ]_{proteoliposome}}{[SPQ]_0} \text{ (Equation 3)}$$

Furthermore, the plot of H^+ efflux versus time was used to determine the initial rate of proton transport (V) in mM/s. This rate was corrected for liposome internal volume to yield V' in nmol/s with equation 3 [7, 68].

$$V'(nmol/s) = V\ (mM/s) \times internal\ volume\ (\mu L) \text{ (Equation 4)}$$

The rate was corrected for non-specific proton leakage by subtracting the calculated V' in nmol/s for blank liposomes and subtracting it from the V' of proteoliposome. This subtracted rate was further corrected for total protein content in proteoliposomes, and the final rate of proton transport was reported as $umol.min^{-1}$.mg $protein^{-1}$ [7, 68].

For inhibition assays, 500 μM ATP was added to 40 μL proteoliposome in 1.96 mL EB and stirred for 2 min. After that, 100 μM PA and 1 μM valinomycin were added and change in SPQ fluorescence signal was measured [7]. All calibrations, as well as the rate of proton transport in the presence of ATP were calculated as described in this section.

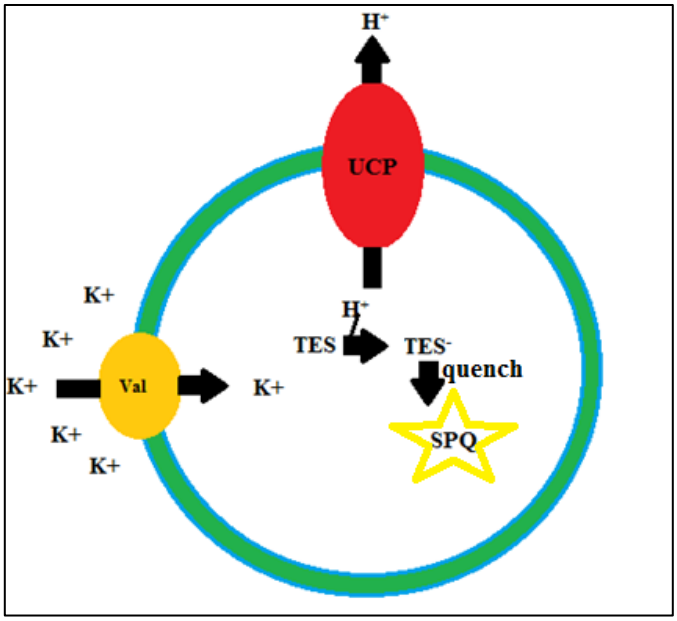

Figure 12: Schematic illustration of the proton transport assay. This assay was set up for the internal compartment of proteoliposomes to contain an internal buffer, SPQ fluorescent probe, and the protonated form of TES buffer. Outside the proteoliposome was an external buffer that had a high concentration of potassium (K^+). Despite the difference in buffer composition, the ionic strength and pH of both buffers were the same so that osmotic balance was maintained before ion flux was initiated with valinomycin (Val). Once valinomycin was added the K^+ gradient triggered the influx of K^+ into proteoliposome. This resulted in the build-up of positive charges inside the proteoliposome and allowed fatty acid activated UCP2 protein to transport protons out of the proteoliposome. H^+ efflux by UCP2 caused the deprotonation of TES to TES^- that quenched the SPQ fluorescence signal [66].

3.2.13. Quantification of Total Protein by Modified Lowry Assay

Modified Lowry assay was used to measure the concentration of purified UCP2 proteins, as well as the final concentration of UCP2 in proteoliposomes. Briefly, purified proteins (20 µL and 40 µL), proteoliposomes (130 µL and 150 µL), and BSA standards were diluted to 1 mL in ultrapure water. After which, 100 µL of 0.15% (w/v) of sodium deoxycholate (DOC) and 100 µL trichoroacetic acid (TCA) were added to precipitate the proteins for 10 min at room temperature (RT). The protein precipitates were centrifuged at 15000 rpm, 4^{o}C for 10 min and pellets were thoroughly resuspended in 25 µL of 20% (w/v) SDS. Next, 100 µL of reagent A'

from Bio-Rad RC DC Protein Assay kit (Bio-Rad) was added to the suspension and vortexed. The solution was sonicated in a water bath for 5min, cooled at RT for 3 min, and sonicated again for 2 min. Afterwards, 800 μL of reagent B was added to sonicated samples before a 30 min incubation at 4 ^{o}C. Lastly, 300 μL of each sample was transferred to a microplate and placed into a microplate reader (Varian) for absorbance measurement at 750 nm.

CHAPTER 4 – RESULTS

4.1. Mutation of UCP2 cDNA with Overlap Extension PCR

The main objective of this research project was to understand the mechanism of ion transport in UCP2. To achieve this objective, lysine residues in the matrix network were changed to glutamine so that the role of these residues on the ion transport activity through their salt bridge interactions in the matrix network of the protein could be examined.

In order to accomplish the above goal, the first step was to introduce three single mutations and one double mutation denoted by the proteins: K38Q, K141Q, K239Q, and K38Q/K239Q into the UCP2 cDNA via overlap extension PCR. The double mutant cDNA was generated to study the impact of losing two salt bridge interactions in the matrix network on UCP2 ion transport activity. Overlap extension PCR technique used three rounds of PCR to create each mutant gene. The double mutant was created by using the K38Q cDNA as the template in a separate overlap extension PCR reaction. To verify that the correct length of nucleotide base pairs was amplified in each round of PCR, the gel purified products of PCR reactions: 1, 2, and 3, were visualized on a 1% agarose gel stained with ethidium bromide. As evident in Figures 13A and 13B, the bands next to the 1 kb DNA ladder represents the full-length UCP2 cDNA. The size of UCP2 cDNA was ~1.05 kb.

Once the mutant genes were produced, the products were cloned into a pET26b(+) vector and transformed into DH5α cells. The recombinant constructs were isolated from bacterial cells and digested with NcoI-HF and HindIII-HF restriction enzymes to confirm the gene products were inserted into the vector. The digested products were loaded onto a 1% agarose gel to identify the bands at ~5.36 kb and ~1.05 kb that corresponded to the size of vector and UCP2 gene respectively (Figure 14A and 14B). Undigested recombinant vector (~6.41 kb) was run

along with the digested constructs to ensure the digested DNA bands observed on the agarose gel were due to restriction enzyme activity [72].

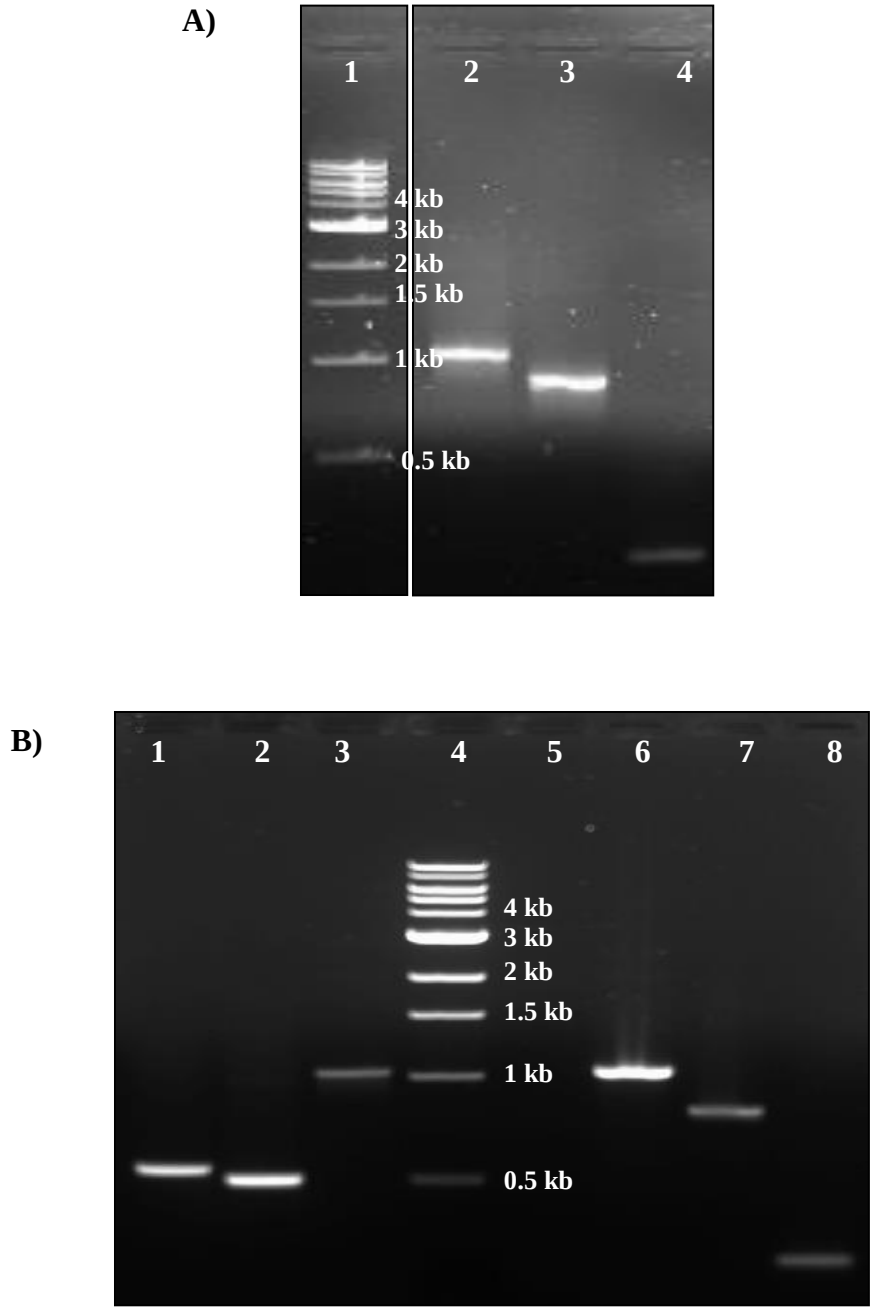

Figure 13: 1% Agarose gel for the overlap extension PCR products used to create the UCP2 mutant cDNAs. A) Lane 1 represents the 1kb DNA ladder, lane 2 represents K38Q PCR reaction #3 (~1.05 kb), lane 3 represents K38Q PCR reaction #2 (~0.7 kb), and lane 4 represents K38Q PCR reaction #3 (~0.35 kb). **B)** Lane 1 represents K141Q PCR reaction #2 (~0.55 kb), lane 2 represents K141Q PCR reaction #1 (~0.5 kb), lane 3 represents K141Q reaction #3 (~1.05 kb); Lanes 6-8 represent K239Q PCR reactions: #3 (~1.05 kb), #1 (~0.8 kb), and #2 (~0.25 kb) respectively.

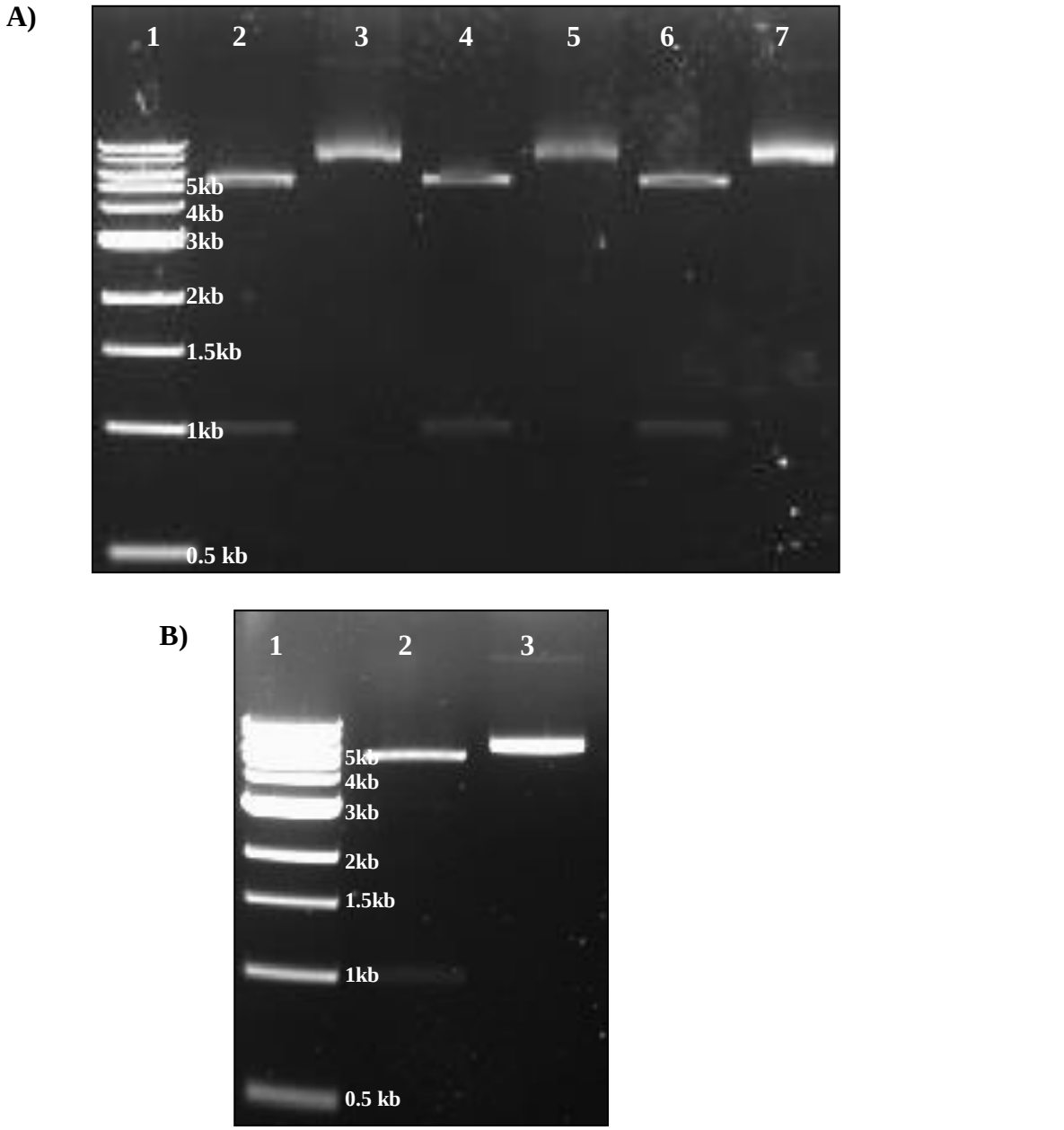

Figure 14: 1% Agarose gel for digested pET26b(+):UCP2-mutant constructs.
A) Digested and undigested pET26: UCP2-K38Q, K141Q and K239Q cDNA respectively. The undigested recombinant vectors were loaded onto the gel as a control: Lane 1 represents DNA ladder, lanes 2-7 represent the cut and uncut recombinant vectors for K38Q, K141Q, and K239Q, respectively. **B)** Restriction digest results for pET2b(+):UCP2-K38Q/K239. In both gels, the DNA band at ~1.05 kb represents the mutant cDNA while the band at ~5 kb indicates the digested vector. The controls had a DNA band above 5 kb which represented the uncut recombinant vector.

As soon as the DH5α cells were confirmed to contain the UCP2 mutant constructs, the recombinant vectors were isolated from the cells and sequenced at the TCAG DNA sequencing facility. The sequenced cDNA confirmed the appropriate mutations were incorporated into the UCP2 cDNA with overlap extension PCR. The nucleotide sequence of the mutants was aligned with wild type UCP2 gene sequence in the NCBI nucleotide blast database [76]. Shown in Figures 15 and 16 are the aligned nucleotide sequences for the mutants with the substituted codons highlighted in black boxes; AAA:CAA for K38Q mutation, and AAG:CAG for K141Q, and AAG:CAG K239Q.

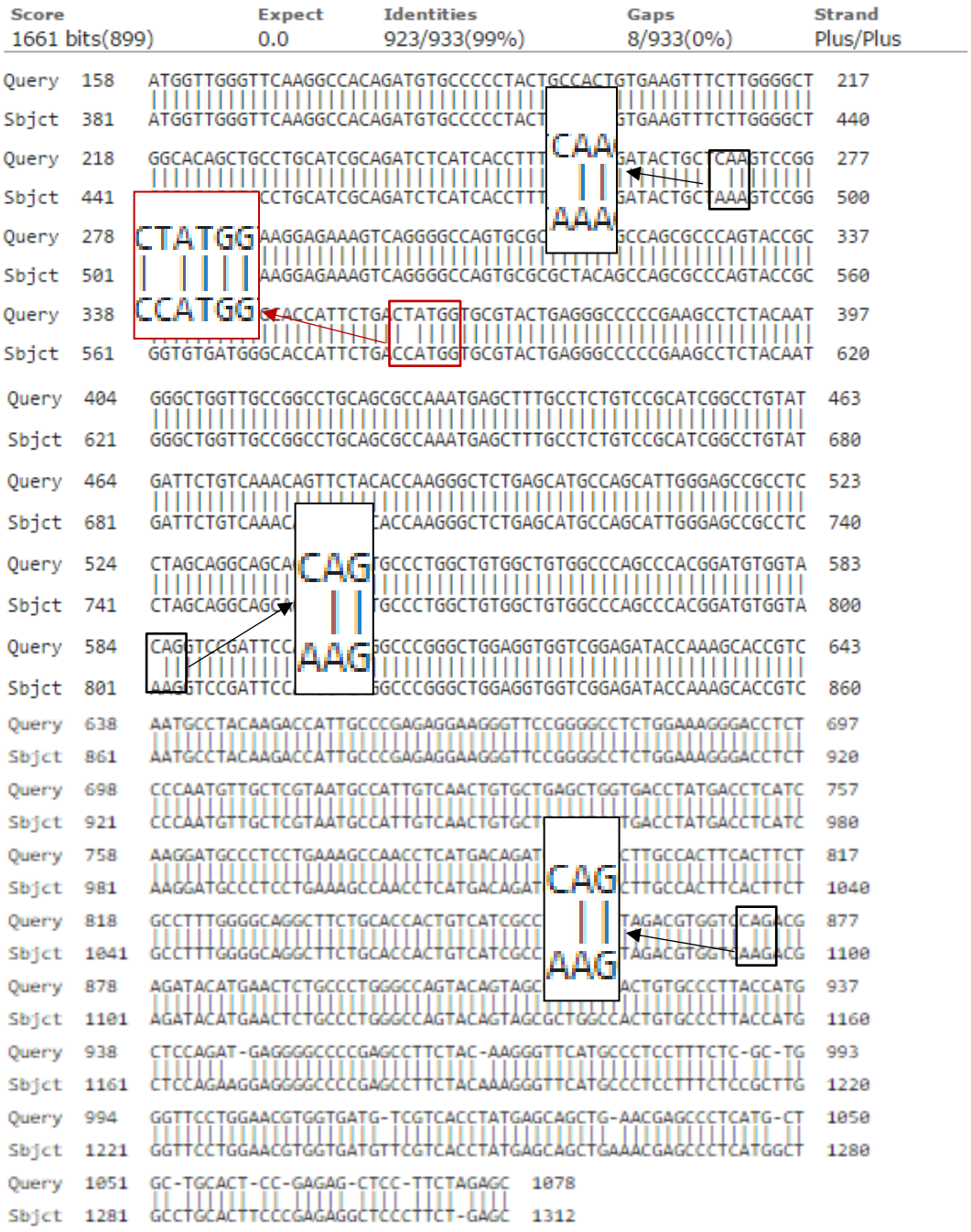

Figure 15: DNA sequencing Results of K38Q, K141Q, and K239Q Primed with T7 Forward Primer: Sequence alignment of PCR amplified single mutant genes (query) was aligned with the UCP2 wild type gene (subject) in the NCBI nucleotide blast database [76]. The desired mutations were: AAA:CAA for K38Q mutation, and AAG:CAG for both K141Q and K239Q (black boxes). The red box indicates the silent mutation introduced into the wild type UCP2 gene to knock out the endogenous NcoI site. This mutation ensured the cDNA remained intact when digested with NcoI and HindIII restriction enzymes before ligating into the pET26b(+) vector.

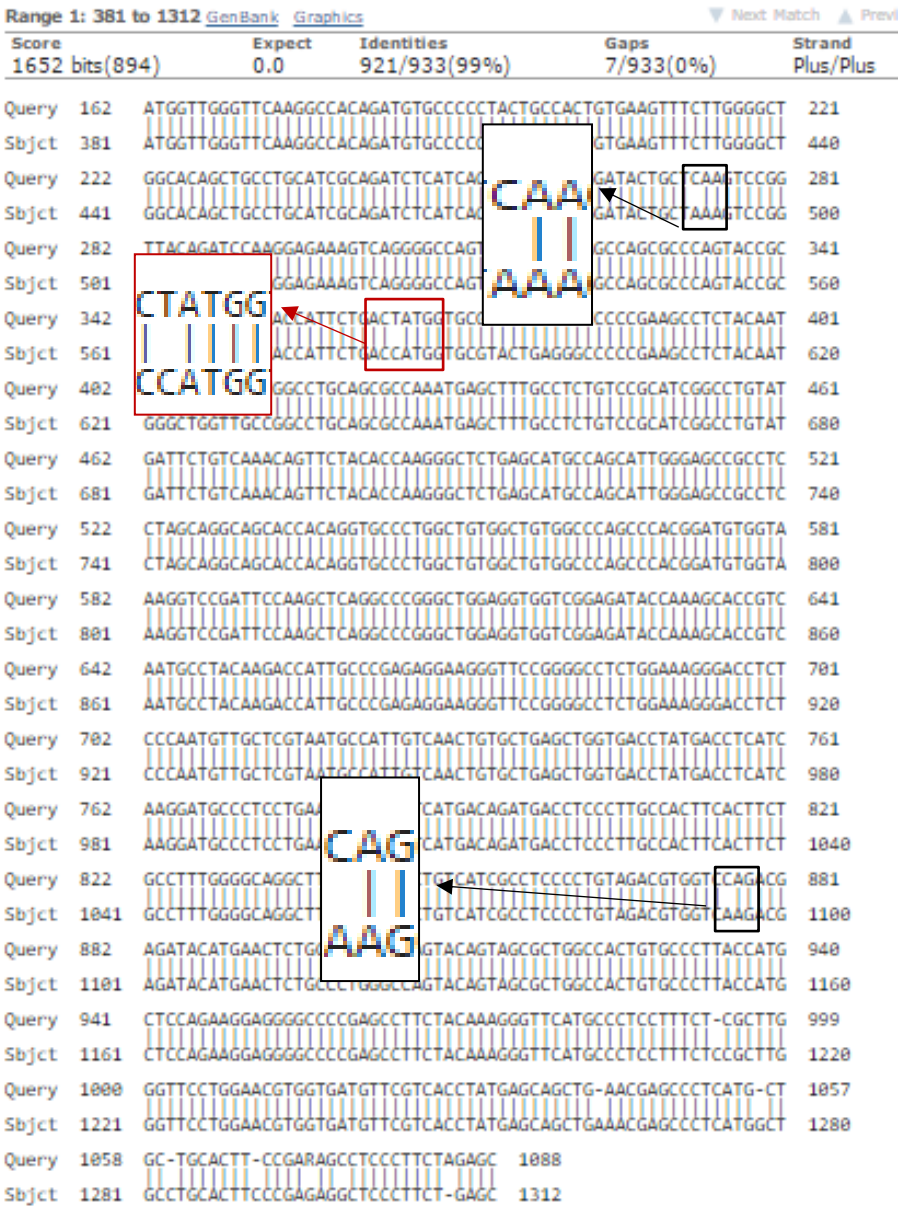

Figure 16: Results for pET26(+):UCP2-K38Q/K239Q Primed with T7 Forward Primer. K38Q/K239Q nucleotide sequence (query) was aligned with the UCP2 wild type gene sequence (subject) in the NCBI nucleotide blast database [76]. The desired mutations were: AAA:CAA for K38Q mutation AAG:CAG K239Q, as indicated by the black boxes. The red box highlightes the knocked out endogenous NcoI restriction site.

Once the cDNAs of the pET26b(+):UCP2 mutant constructs were confirmed to have the required the mutation, the recombinant vectors were isolated from DH5α and transformed into BL21 CD^+ with heat shock. A restriction double digest of the recombinant vector verified the presence of the constructs in BL21 CD^+ cells due to the bands at ~1.05 kb (UCP2 cDNA) and ~5 kb (vector) on lanes 2, 4, 6, and 8 (Figure 17). BL21 CD^+ has two endogenous plasmids one of which is a pSC101-based plasmid (~4.7 kb) that encodes a streptomycin resistance gene as well as an HindIII cut site [77]. The other plasmid is a pACYC-based plasmid (~3.5 kb) that has a chloramphenicol resistant gene and both HindIII and NcoI restriction sites [77]. Therefore, the bands at ~1.4 kb and ~1.9 kb correspond to the digested pACYC plasmid. On the other hand, the band at ~5 kb may be a combination of the digested pSC101 and pET26b(+) vectors because they are relatively similar in size.

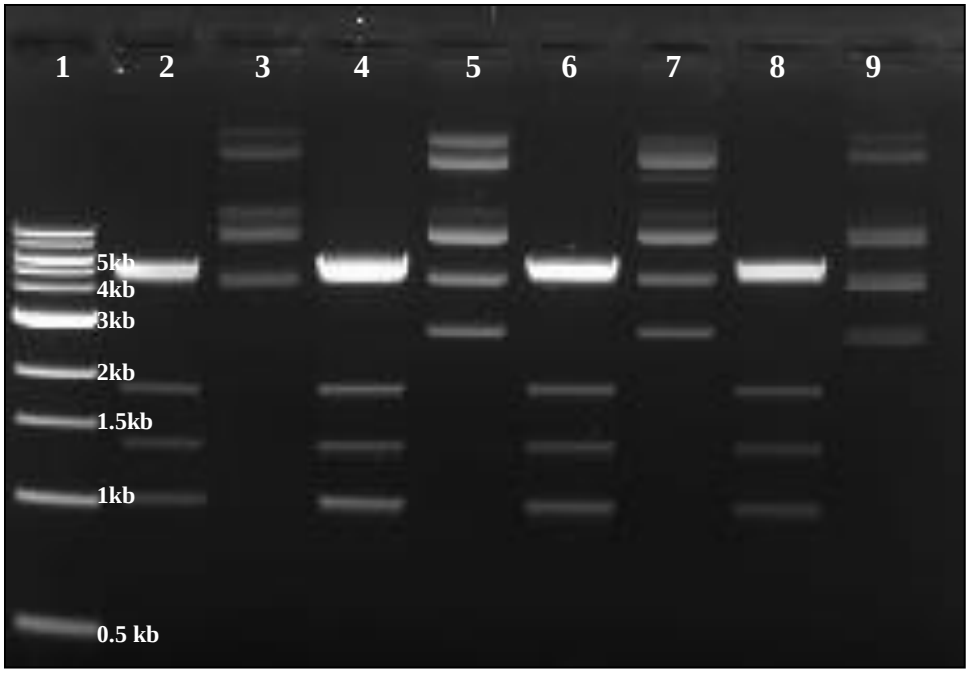

Figure 17: 1% Agarose gel for restriction enzyme digest of UCP2 mutant constructs isolated from BL21-CodonPlus (DE3)-RIPL cells. Lane 1 represents the 1 kb DNA ladder. Lanes 2 - 9 represent the digested and undigested recombinant vectors: pET26:UCP2-K38Q, pET26b(+):UCP2-K141Q, pET26b(+):UCP2-K239Q, and pET26b(+):UCP2-K38Q/K239Q. All digested recombinant vectors have a band at ~1 kb that represents the cDNA while that band at ~5 kb represents the pET26b(+) vector. The bands at ~5 kb may also represent the linearized pSC101 while the bands at ~1.4 kb and ~1.9 kb represent the digested pACYC plasmid. The undigested plasmids (lanes 3, 5, 7, and 9) indicate the endogenous BL21 CD^+ plasmids at ~4.7 kb and ~3.5 kb, and also the recombinant pET26b(+) vector at ~5 kb [77].

4.2. Expression of UCP2 Proteins in Bacterial Membranes and Purification with IMAC

Overexpression of UCP2 mutant and native proteins in BL21 CD^+ cells was initiated with auto-induction as described in 3.2.4. Protein expression was directed towards the bacterial inner membrane with a pelB signal peptide encoded by the pET26b(+) vector [68]. The signal peptide targets secreted proteins to the periplasmic space via the Sec translocase pathway [49, 50]. However, due to hydrophobic interactions, the TM segments of UCP2 proteins are inserted into the bacterial membrane during translocation [78]. The bacterial membrane enriched with UCP2

proteins was separated from soluble and aggregated (inclusion bodies) proteins after cell lysis and ultracentrifugation. In a previous study, SDS-PAGE analysis and NADH oxidase activity assays confirmed that the bacterial membranes were enriched with UCP2 proteins [79].

Once the proteins were extracted from bacterial membranes using detergent solubilization, the previously established purification protocol [68, 79] proved insufficient in purifying UCP2 from unwanted proteins. The SDS-PAGE for the purified mutant and native proteins indicated a band at ~33 kDa represented the UCP2, while other protein bands at: ~250 kDa, ~150 kDa, ~75 kDa, ~50 kDa, ~27 kDa, and ~17 kDa were also observed on gel (Figure 18). The MW proteins at ~150 kDa and ~75kDa were suspected to be dimer and tetrameric forms of the proteins because a gradual dissociation to monomers (~33 kDa) was observed when purified UCP2 was titrated with increasing SDS concentrations [79]. On the other hand, the lower MW proteins at ~27 kDa and ~17 kDa might be truncated forms of UCP2 protein.

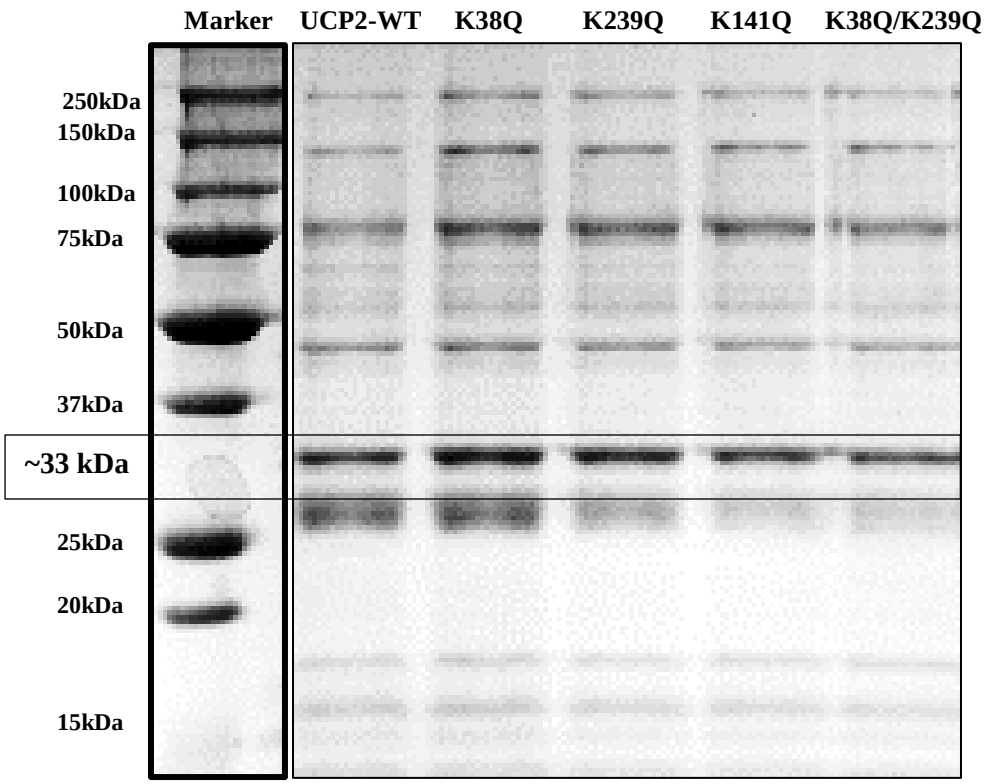

Figure 18: SDS-PAGE of IMAC purified and desalted UCP2 and mutant proteins. The purified proteins were resolved on a 12% resolving SDS gel, stained with Coomassie Brilliant Blue. The box highlights the ~33 kDa band for UCP2 monomer. Higher and lower molecular weight protein bands present on the gel could be multimeric forms of UCP2 or degraded protein contaminants respectively.

To improve protein purity, two wash buffers that contained 75 mM and 100 mM imidazole were applied onto the IMAC column after the column was washed with 30 mM imidazole wash buffer. After that, the desired proteins were eluted with 400 mM imidazole. Although most protein contaminants were removed from the column by the wash buffers, some UCP2 proteins also eluted in these fractions which decreased the concentration of UCP2 in 400 mM fractions (most pure) (Figure 19). Interestingly, UCP2 monomers were the major

constituent in the 400 mM imidazole fractions while the multimeric and truncated forms of UCP2 were eluted in the wash buffers.

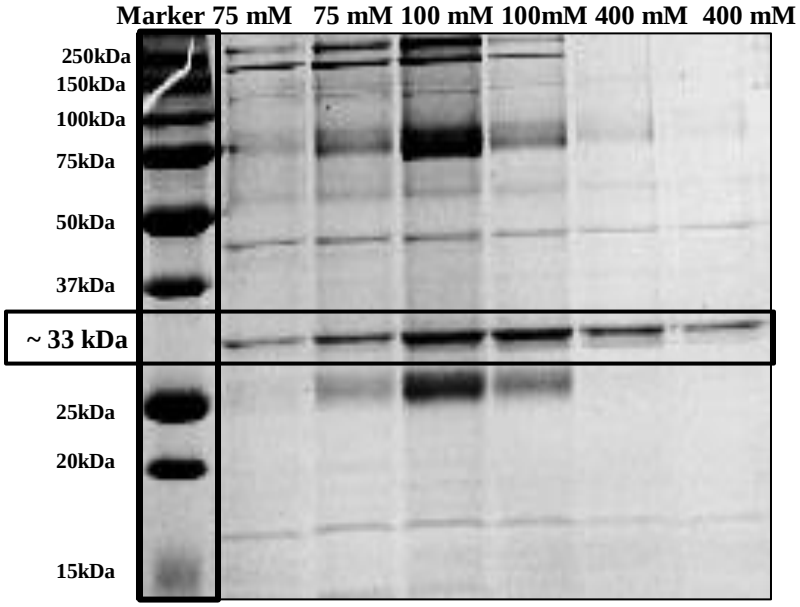

Figure 19: Purification of UCP2 native protein with step imidazole gradient.
The SDS-PAGE shows that most of the higher and lower MW proteins were eluted with 75 mM and 100 mM. The fractions eluted with 400 mM imidazole contained the UCP2 monomer with the highest purity.

Although UCP2 monomers were obtained in good purity, the protein concentration in the fractions eluted with 400 mM imidazole was insufficient for downstream applications. Therefore, to maximize the yield and purity of UCP2 and its mutants, 30 mM imidazole and 75 mM imidazole were utilized to remove most of the protein contaminants, while 400 mM imidazole eluted the dominantly monomeric UCP2 proteins from the IMAC column. Based on the SDS-PAGE gel in Figure 20, majority of the higher and lower MW bands were eluted in the 75 mM imidazole wash buffer with minimal loss of UCP2 monomers in these fractions. The 400 mM imidazole containing buffer eluted any remaining contaminants and some UCP2

monomers in first two fractions while later fractions contained substantial amounts of UCP2 monomers with a high degree of purity.

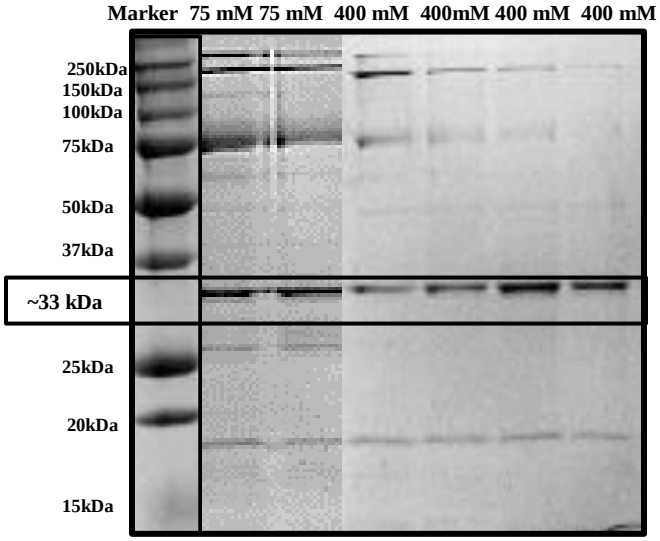

Figure 20: SDS-PAGE for UCP2 wild type purification with 30 mM, 75 mM, and 400 mM imidazole concentrations. Only the UCP2 fractions eluted with 75 mM and 400 mM are shown on the SDS gel. Most of the higher MW proteins eluted in the 75 mM imidazole wash buffer while the UCP2 monomer was obtained in fractions eluted 400 mM imidazole elution buffer. The proteins in these fractions had a higher degree of purity and concentration that was sufficient for biophysical analysis.

Since the modified protocol purified UCP2 wild type with adequate purity and yield, this protocol was also used to purify the single and double mutant proteins. The purified proteins were further desalted in a size exclusion column to remove any imidazole that may interfere with spectroscopic studies. The desalted proteins were separated on an SDS-PAGE and the UCP2 monomer at ~33 kDa was identified for all proteins. However, the K38Q/K239Q (double mutant (DM)) still had higher molecular weight bands that indicated the presence of dimer and tetrameric forms of the protein (Figure 21). In addition, the MW protein ~27 kDa was also identified in DM. The band at ~17 kDa present in all proteins was approximately half the size of

the UCP2 monomer. Therefore, this protein band was indicated UCP2 degradation by protease enzymes that were released from the host cell during cell lysis [80].

The identity of each UCP2 protein was verified on a Western blot that was probed with an anti-UCP1/2/3 polyclonal antibody (section 3.2.8.). The UCP2 monomer was detected at ~33kDa while the suspected degraded protein was indicated at ~17 kDa for UCP2-WT and DM protein (Figure 22).

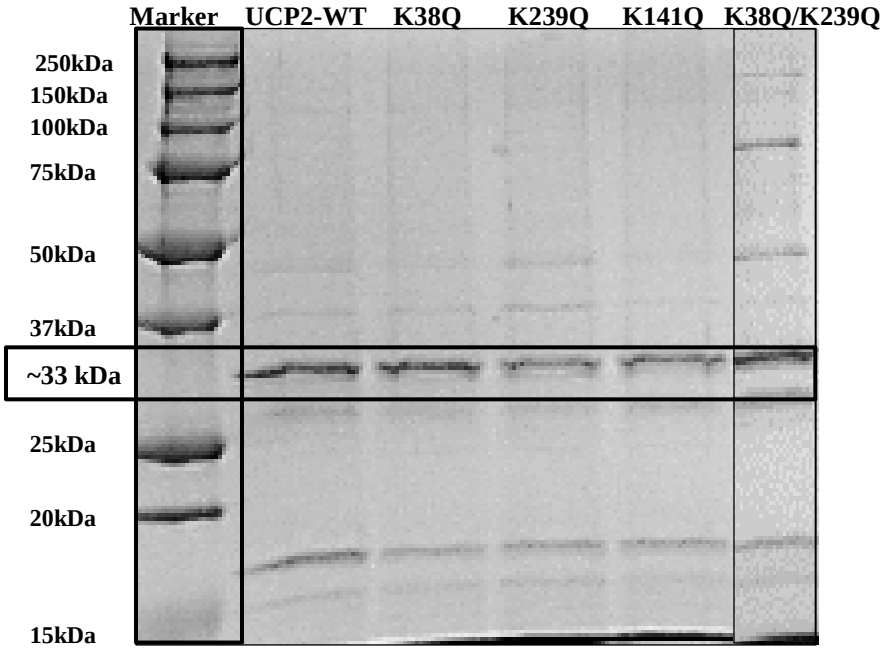

Figure 21: SDS-PAGE results for purified UCP2 wild type (WT) and mutant protein: All proteins were expressed in bacterial membranes and purified with IMAC in 1% OG. Purified proteins were resolved in a 12% SDS-PAGE gel stained with Coomassie Brilliant Blue. The sizes of the Marker are shown in kDa. The band at ~33kDa represents the UCP2 monomer. UCP2 dimer at ~75 kDa and tetramer at ~150 kDa were observed for DM.

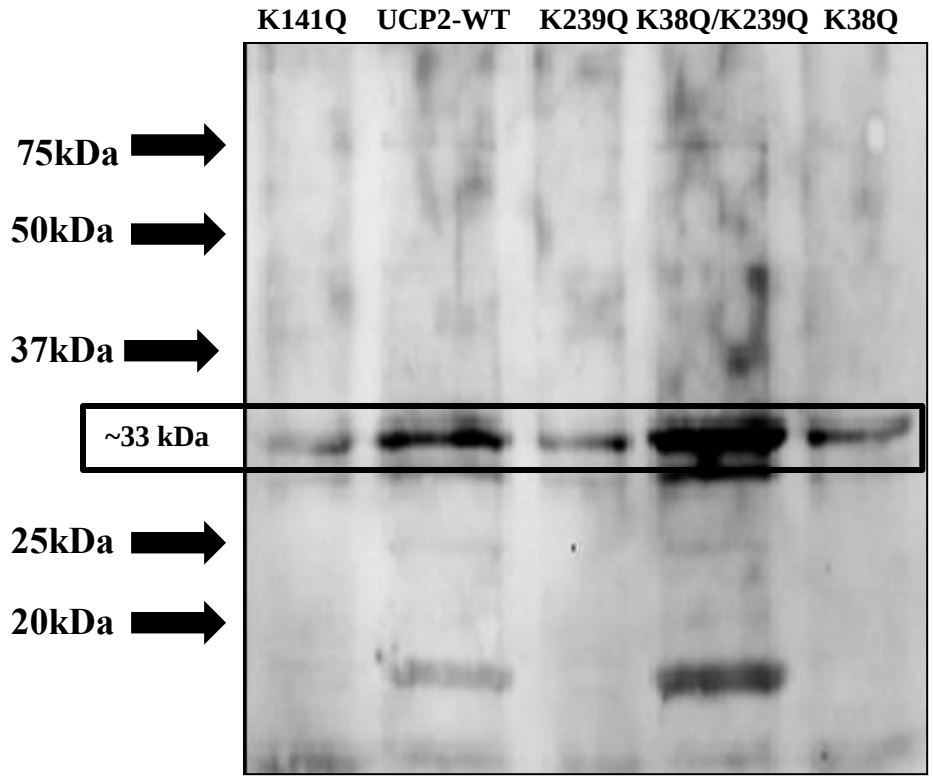

Figure 22: Western blot detection of UCP2 recombinant proteins: The proteins were identified with an anti-UCP1/2/3 polyclonal primary antibody raised in rabbit. The Western blot was detected with chemiluminescence and the UCP2 protein ~33kDa was observed.

4.3. Far-UV CD Measurements of UCP2 and Mutant Proteins

Far-UV CD has previously shown that UCPs have predominantly α-helical conformations in detergent micelles and phospholipid vesicles [7, 68, 79, 81]. In this study, the far-UV CD spectra determined the conformation of the purified proteins in detergent (1% OG) micelles. Blank measurements (buffer containing 1% OG) were subtracted from the proteins CD spectra to correct for noise interferences induced by buffer ions and detergent micelles [63]. Subsequently, the corrected spectra were converted to mean residue ellipticity which normalized the spectra with respect to the cuvette path-length and concentration of proteins used in each measurement [63]. The overall conformations of the mutant and native proteins were α-helical with local minima at ~208-210nm nm and ~220- 222 nm, as well as a local maximum at 195 nm

(not fully observed due to noise at wavelengths below 195nm) (Figure 23). The native UCP2 had a negative minima ellipticity at 210 nm and 220 nm. The overlapped CD spectra for K38Q and K239Q indicated structural similarities for both proteins. Compared to native UCP2 however, these proteins had less negative ellipticities at 210 nm and 220nm. Although the negative minima at 220 nm red shifted to 222 nm in K38Q/K239Q (DM), the ellipticities at 210 nm and 220 nm for the DM were the least negative of all the proteins. Meanwhile the CD spectra for K141Q revealed that the negative ellipticity at 210 nm blue-shifted to 208nm while the shoulder at 220 nm was relaxed, less negative, and blue shifted toward 219 nm.

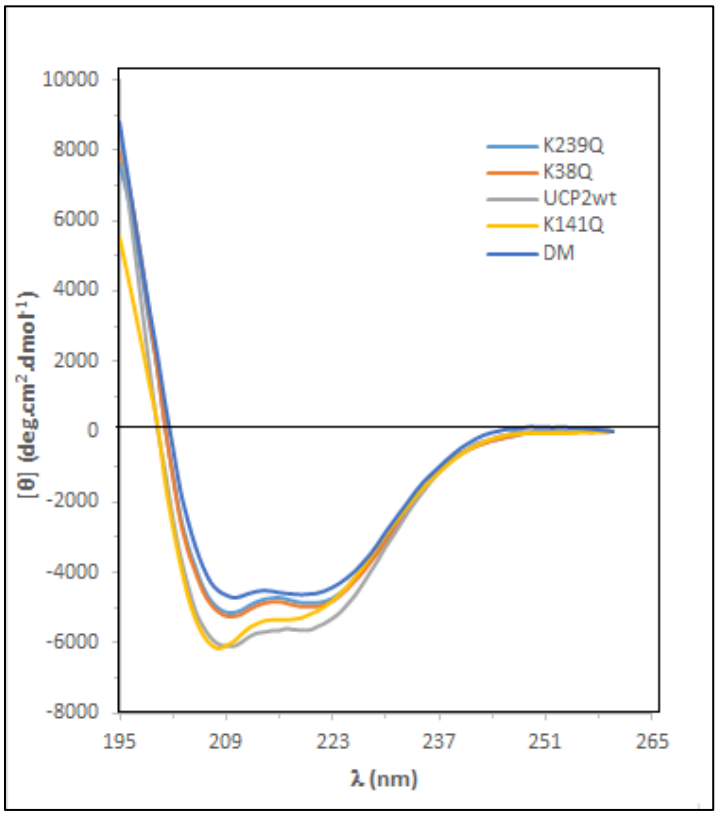

Figure 23: Far-UV CD spectra for mutant and native UCP2 in detergent micelles. The CD spectrum for each protein was the average of 3 scans in mean residue ellipticity K38Q/K239Q mutant is indicated as DM in the above spectra. All proteins had an overall α-helical conformation in 20mM Tris-HCl pH 8. The protein concentrations used for each measurement range from 5 μM – 8 μM.

The molar ellipticity ratio ($\theta_{208\ nm}/\theta_{222\ nm}$) estimates the degree of inter-helical packing in proteins [68]. A $\theta_{208\ nm}/\theta_{222\ nm}$ ratio ≥ 1 indicates a densely packed helical conformation while a loosely packed or more relaxed helical conformation is observed at ratios < 1 [68]. All UCP2 proteins except the DM had a more negative ellipticity at 208 than 222 nm (Table 4). Hence, the $\theta_{208\ nm}/\theta_{222\ nm}$ (Table 4) identified loosely packed helical conformation for UCP2 and single mutant proteins and a more densely packed conformation for the DM.

The percentage α-helix composition in each protein was analyzed with CDSSTR on the Dichroweb website and results of the deconvoluted data are shown in Table 4. Based on the deconvoluted data, UCP2-WT has the highest helical content, followed by K38Q, K239Q, K38Q/K239Q and K141Q, respectively.

Table 4: Secondary structure composition of UCP2 proteins in detergent micelles. The CDSSTR program on the Dichroweb website was used to determine the percentage α-helix content from the CD spectra in molar ellipticity [74, 75]. The ratio of $\theta_{208}/\theta_{222}$ indicates the degree of helical packing in the proteins.

Protein	α-Helix (%)	θ_{222nm}	θ_{208nm}	Ratio of $\theta_{208}/\theta_{222}$
UCP2-WT	23	5440	6093	1.12
K38Q	20	4952	5272	1.06
K239Q	20	4840	5160	1.06
K141Q	17	4993	61935	1.24
K38Q/K239Q	20	4532	4543	0.99

4.4. Liposome Size Determination with DLS

The purified proteins were reconstituted into phosphotidylcholine vesicles to compare ion flux measurements. DLS measured the size and homogeneity of the proteoliposomes to ensure LUVs (100 nm – 1 μM diameter) were prepared and vesicles were stable during proton transport measurements. Protein-free liposomes (blank liposomes) were made in parallel to preoteoliposome to serve as a control for ion transport measurements. In general, the sizes of

each proteoliposome were less than the blank; possibly the incorporated protein induced a curvature stress on the vesicle that decreased the size of the proteoliposomes (Table 5) [82]. A percent polydispersity (%PD) ≤ 20% indicated a relatively monodisperse size distribution while a %PD above 20 identified polydispserse size populations [83]. Hence, the size population of UCP2-WT, K38Q, and K239Q proteoliposomes were monodisperse while, K141Q, DM and protein-free liposomes were ranged from medium to polydisperse size distributions (Table 5).

Table 5: Average diameter (nm) of liposome and proteoliposome used in ion transport measurements: The sizes below are the average of three independent preparations. Protein-free liposomes (blank liposome) was prepared along with the proteoliposomes. The standard error of the mean (SEM) is reported along with the sizes, while the dispersity of the vesicles is represented in percent polydispersity (%PD).

Sample	Average Diameter ± SEM	% PD
Blank	234 ± 8	31
UCP2-WT	212 ± 12	16
K38Q	199 ± 4	18
K239Q	215 ± 7	20
K141Q	210 ± 5	31
K38Q/K239Q	204 ± 13	23

4.5 Proton Transport Measurements for Native and Mutant UCP2

The rates of fatty acid-mediated proton transport in mutants were compared to the native UCP2. Proton transport measurements were obtained for reconstituted UCP2 wild type and mutant proteins as stated in 3.2.12 [66, 68]. Shown in Figure 24 is the proton efflux (in mM) mediated by the proteins (black curve) across phospholipid vesicles after valinomycin was added to the assay. Proton efflux across protein-free liposomes (red curve) was also measured to account for non-specific leakage induced by the liposome. Overall, each protein had a higher proton efflux than the blank liposome. The initial rates of proton transport were calculated within the first 25 s after valinomycin addition and corrected for non-specific leakage and total protein

content. The calculated proton flux was reported as μmol.min^{-1}.mg protein^{-1} (Table 6). As expected, UCP2-WT had the highest proton flux compared to the mutant proteins. K38Q and K239Q had similar transport rates but compared to UCP2-WT, these rates were ~36% and ~34% less. The proton flux for K141Q and DM were ~70% and ~71% less than the wild type UCP2.

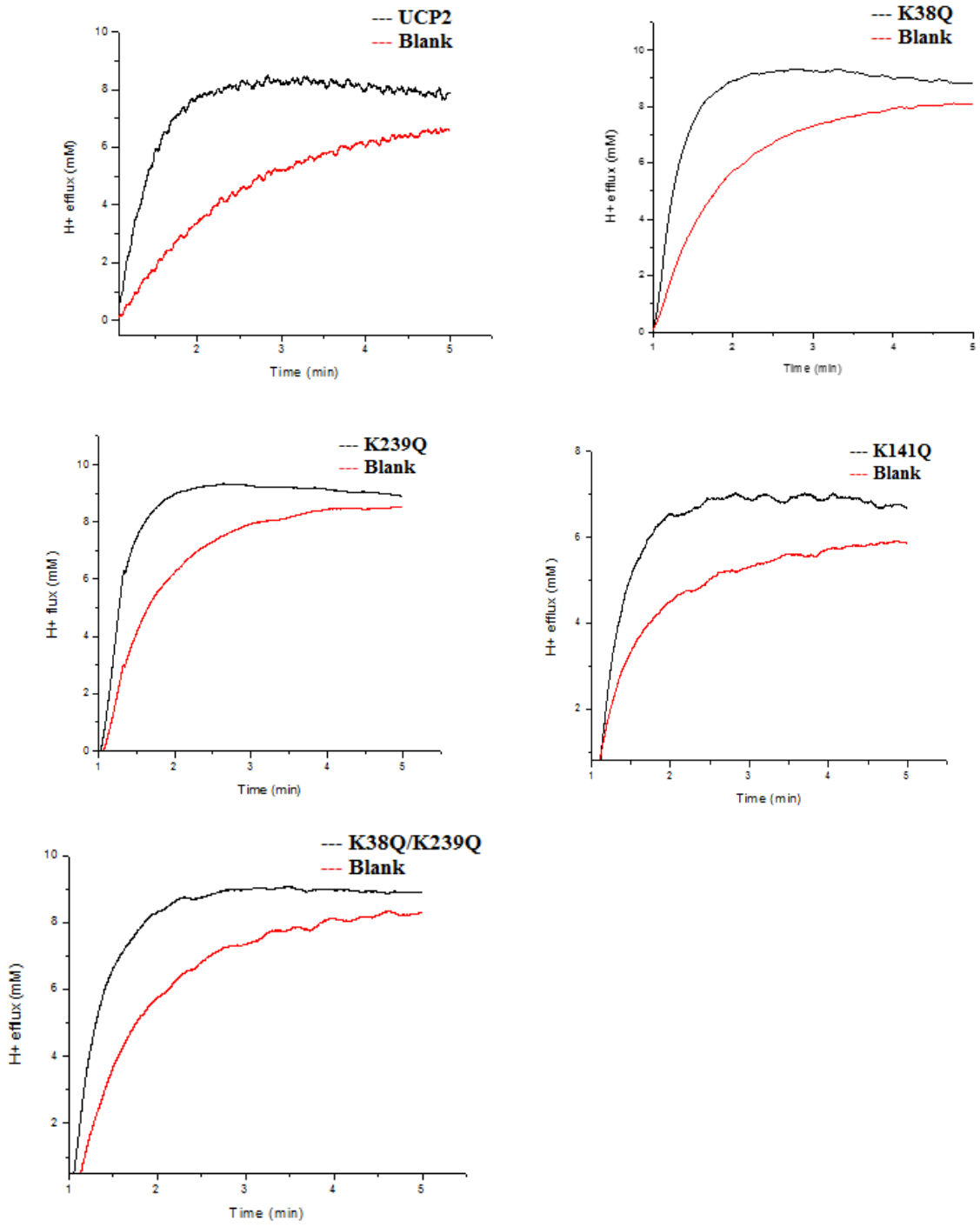

Figure 24: Fatty acid-mediated proton transport by native and mutant UCP2 across phospholipid vesicles. Non-specific proton efflux in protein-free blank liposomes (red) was less than the proton efflux in UCP2 proteoliposomes (black). Proton efflux was indirectly measured by quenching SPQ fluorescence with the TES anion. The above plot is the average of 3 independents measurements and the total protein concentration was quantified with modified Lowry assay. The protein concentration in proteoliposomes ranged from 0.24 μM – 0.5 μM.

Table 6: Corrected proton flux for wild type and mutant UCP2: The reported transport rate for each protein are the average rates from three independent measurements ± standard errors of the mean (SEM). The final protein content was 0.24 – 0.5μM.

Protein	Proton flux in μmol min^{-1}(mg protein)$^{-1}$ ± SEM
UCP2-WT	42.5 ± 2.8
K38Q	27.5 ±3.6
K239Q	28.2 ±3.4
K141Q	13.8 ±0.8
K38Q/K239Q(DM)	12 ±1.2

4.6. Inhibition of Fatty Acid-Mediated UCP2 Proton Transport

Purine nucleotides are known inhibitors of UCP ion transport function as confirmed by multiple inhibition assays in past studies [7, 68]. In this study, the impact of ATP on UCP2 (and mutants) proton transport activity was measured by incubating each proteoliposome with 500 μM ATP for 2 min before valinomycin was added to initiate proton transport [7, 68]. The proton transport rate was also measured in the absence of ATP for comparison (Figure 25). Shown in Figure 25 are the observed proton efflux (mM) as a function of time for UCP2 proteins in the presence (red line) and absence (black line) of ATP. The initial rate of proton transport (with and without ATP) was corrected for non-specific leakage and protein content in the liposome. The percentage decreases in the initial rate of proton transport due to the interaction of ATP with the proteins are listed in Table 7. In the presence of ATP, the UCP2-WT proton flux decreased by 14% which was indicative of partial nucleotide inhibition [7]. The proton transport rates of the mutants were inhibited by ATP to varying extents; K239Q, K141Q and DM proton transport rates decreased by less than 7% while K38Q proton transport rate decreased by 38%. These preliminary results indicate that the interaction of ATP with UCP2 proteins led to a more decreased proton transport rate in K38Q compared to the UCP2-WT and other mutant proteins. However, further experiments need to be performed to verify this observation.

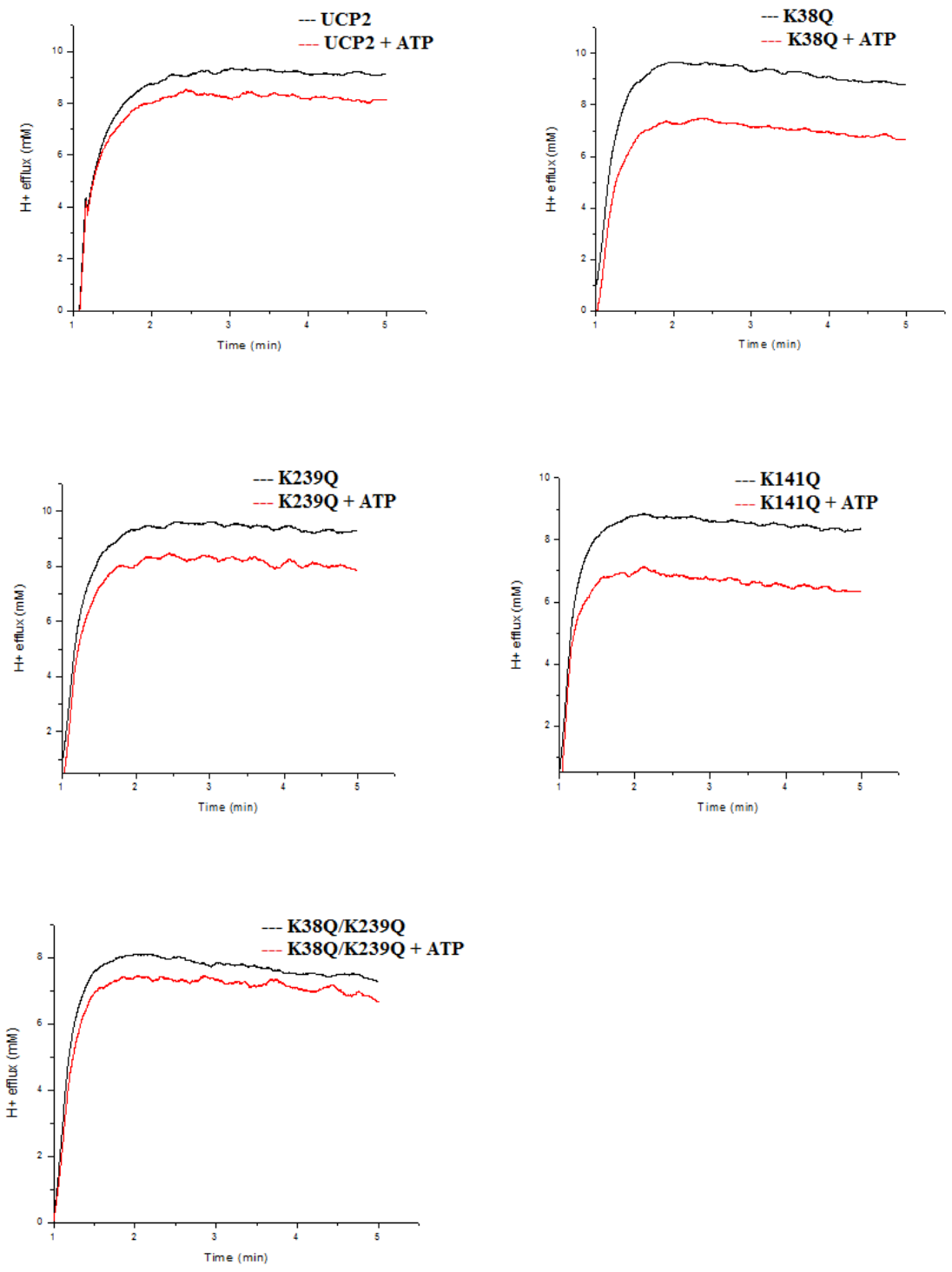

Figure 25: Inhibition of UCP2 and mutant proton efflux by ATP. Proton transport assay was performed as described in section (4.1.12). Total protein content was quantified with modified Lowry assay. The concentration of protein in each proteoliposome ranged from 0.35µM – 0.55µM.

Table 7: Rate of proton flux in the absence and presence of purine nucleotide: Proton transport measurements were triggered after incubating the liposomes with 500μM ATP for 2min. The reported percent decrease rate is the relative change in proton transport rate in the absence and presence of inhibitor.

Protein	Proton transport rate without ATP (μmol min^{-1}(mg protein)$^{-1}$)	Proton transport rate with ATP (μmol min^{-1}(mg protein)$^{-1}$)	% Decrease in Rate of Proton Transport
UCP2-WT	41	35	14
K38Q	21.7	13	38
K239Q	21.7	21	3.2
K141Q	15.3	14.3	6.5
K38Q/K239Q(DM)	13.1	12.6	3.8

CHAPTER 5 – DISCUSSION, CONCLUSION AND FUTURE STUDIES

5.1. Discussion

This thesis addressed the impact of lysine amino acids in the matrix network of UCP2 on the ion transport mechanism of the protein. These lysine residues are proposed to form a salt bridge interaction with oppositely charged amino acids in the matrix network (Figure 6B) [42]. Furthermore, the disruption and formation of this salt bridge interaction induced by a bound substrate could result in substrate translocation through the protein [42]. Using overlap extension PCR and designed primers, mutations were introduced into the UCP2 cDNA to create K38Q, K239Q, K239Q, and K38Q/K239Q (DM) in the recombinant protein. Four mutant proteins were expressed and purified successfully. As expected, the proton transport activity of the mutants was less than the native protein while the effect of these residues on the ATP binding site showed different degrees of proton inhibition. These experimental results provide further insight into the mechanism of proton uncoupling by UCP2 in the mitochondria.

5.1.1. Expression of UCP2 Proteins in Bacterial Membranes

Recombinant membrane proteins that are required for biophysical and structural studies are typically obtained from bacterial systems in large quantities; however, it is often difficult to isolate the protein in their native-folded state [84]. As a result, membrane proteins expressed in *E.coli* are often extracted from insoluble aggregates (inclusion bodies), followed by the labour intensive process of re-folding in detergents that typically yield partially folded proteins [85]. In this study, folded recombinant UCP2 proteins were recovered from bacterial membranes by using a pelB signal peptide that was encoded on the pET26b(+) vector [49]. The signal peptide

targets secreted proteins to the periplasmic space by interacting with a signal recognition particle (SRP) and the membrane embedded Sec translocase complex [78]. When the peptide is fused to the n-terminus of membrane proteins, the hydrophobic interactions between the TM helices and phospholipid bilayer presumably provide an energy barrier that favour the insertion of the protein into the inner mitochondrial membrane while the leader sequence is cleaved by a signal peptidase in the periplasmic space [78].

Another challenging aspect in structural studies of membrane proteins *in vitro,* is the isolation and purification of the folded proteins with high yield and purity. In this research project, overexpressed UCP2 proteins were extracted from bacterial membranes using detergent solubilization [68]. A zwitterionic detergent (LDAO) was used to isolate proteins from the phospholipid bilayer by partitioning into the bacterial membrane and dissociating the lipid-protein complex in the bilayer [86]. Though LDAO facilitated UCP2 extraction from bacterial membranes, the zwitterion may disrupt the native conformation of the protein. Therefore, LDAO was exchanged with an uncharged mild detergent (OG) on the IMAC column [68].

To achieve maximum purity and yield, an imidazole step gradient was used to purify UCP2 proteins in its dominantly monomeric form (~33 kDa) (Figure 21). It was previously proposed that UCP monomers could associate and form oligomeric states in detergent and lipid vesicles [9]. UCP1 and UCP2 were observed to have tetrameric (~150 kDa) conformation on a semi-native gel [79]. This observation was also proved when the tetramer dissociated into dimers (~75 kDa) and monomers (~33 kDa) in high SDS concentrations [68, 79]. A recent study dismissed the notion of an associated stated for UCP1 and claimed the reason for the MW at ~150 kDa was due to a protein-detergent-lipid complex [87]. The authors also hypothesized that cardiolipin was most likely to complex with UCP1 based on isothermal titration calorimetry

(ITC) measurements, and the propensity of cardiolipin to interact with IMM proteins. Despite this observation, results from both studies indicate that UCPs could form lipid-protein-detergent complexes and/or oligomeric complexes.

Oligomers and lower MW proteins (Figure 18) were observed when UCP2 and its mutants were purified with the previously established protocol in our lab [68, 79]. However, when a step imidazole gradient was used, majority of the higher MW proteins (dimer and tetramer) and protein contaminants eluted in lower imidazole concentrations (30 mM, 75 mM and 100 mM) while the UCP2 monomer eluted in the 400 mM imidazole containing elution buffer (Figures 19 and 20). The associated forms of UCP2 eluted in 75 mM and 100 mM fractions because these conformations may have masked the His-tag which hindered its interaction with the Ni-NTA resin [88]. In turn, this enabled the multimeric forms of the protein to elute when low imidazole concentration was added to the column. Coincidentally, the monomer was also present in these fractions which could also indicate insufficient exposure of the His-tag to the Ni-NTA-resin. Despite the loss of UCP2 monomers in fractions eluted with most protein contaminants, a sufficient concentration of monomers was obtained in the 400 mM imidazole eluted fractions (Figure 21). Compared to the native and mutant proteins, the double mutant showed evidence of associated forms as higher MW bands at ~75 kDa and ~150 kDa were identified. In addition to the monomer, a protein band at ~17 kDa was also visible for all UCP2 proteins. This band was suspected to be a degraded form of the protein because the protein was detected for UCP2 and double mutant proteins on a western blot (Figure 22). In all, UCP2 monomers were successfully purified with a high degree of purity and yield; but additional purification steps such as size exclusion chromatography could be employed to further improve the purity of the proteins.

5.1.2. Impact of Mutated Lysine Residues on the Structure of UCP2

Far-UV CD revealed that the secondary structure of the mutant and wild type UCP2 proteins were comparable. All proteins exhibited an overall α-helical conformation in detergent micelles as evident by the local minima at ~208-210 nm and ~220-222 nm in Figure 23. The estimated percentage α-helix composition of UCP2-WT and mutant proteins were also similar as shown in Table 4. UCP2-WT was estimated to be 23% helical which is less than the 63% α-helix composition observed in past studies for UCP2 in detergent [79]. Several strategies can be used to increase the alpha helical composition of membrane proteins, such as purifying the proteins in detergents that stabilize the α-helices and also reconstituting into phospholipid vesicles which was shown in past experiments to induce helical conformations in UCPs [68].

In this study, the local minimum at 208 was more negative than 222 nm and consequently the $\theta_{208}/\theta_{222}$ ratio was above 1 for UCP2-WT and single mutants. Experimental results from a previous study indicated that UCP1, 2, 4, and 5 had a more negative ellipticity at 208 nm compared to 222 nm as well as a molar ellipticity ratio ≥ 1 when increasing SDS concentrations were added to the proteins [68, 79]. It was suggested that the elliptical shifts indicated a change in protein conformation from an oligomeric complex to a monomer and hence, the molar ellipticity ratio (≥ 1) was indicative of a loosely packed alpha helix [68, 69]. Therefore, the more negative ellipticity at 208 nm compared to 222 nm indicated that UCP2-WT and single mutants were mostly monomers as shown on the SDS-PAGE. While the similar negative ellipticties at 208 nm and 222 nm observed for DM represented a mixture of monomers and oligomers as observed on the SDS-PAGE (Figure 23).

The $\theta_{208}/\theta_{222}$ ratio differed for each protein as stated in Table 4. The UCP2-WT had a loose helical packing due to the $\theta_{208}/\theta_{222}$ ratio above 1. Though K38Q and K239Q had similar

ratios and signified similar relaxed helical packing conformations, these ratios were 5% less than UCP2-WT which indicated a less relaxed helical packing for both mutants. Also, the DM exhibited a densely packed helix due to the $\theta_{208}/\theta_{222}$ ratio below 1, while K141Q ratio identified the helical packing of this protein as 10% more relaxed than UCP2-WT (Figure 26). Overall, these results imply that the mutations could have induced a conformational change in the micro-environment around the glutamine residue due to the loss of the salt bridge interactions and as a result altered the helical packing conformation of UCP2.

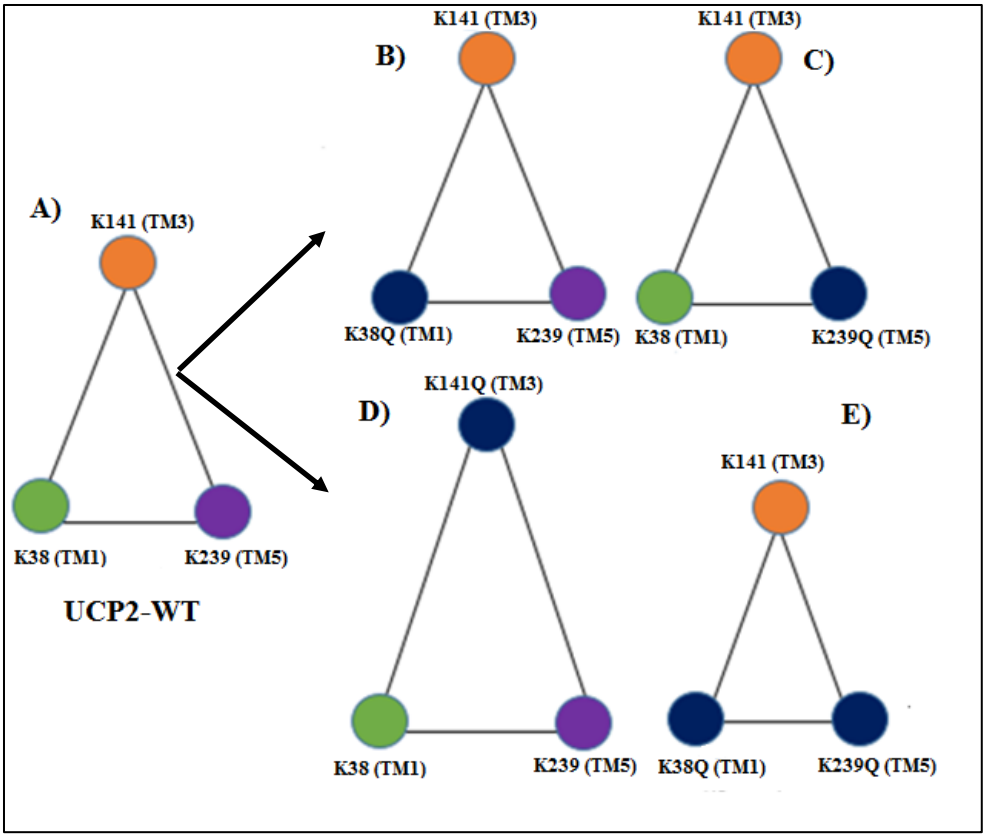

Figure 26: Comparative conformational changes in helical packing of UCP2 and mutants. The above image illustrates the helical packing conformations of UCP2 native and mutant proteins as determined by the shifts in negative ellipticity and the molar ellipticity ratio ($\theta_{208}/\theta_{222}$). The size of the triangles represent the degree of helical packing for the proteins, where a small triangle indicates densely packed helices and a large triangle represents a loose/relaxed helical packing compared to the native UCP2. The green, purple and orange circles represents K38 (TM1), K141 (TM3), and K239 (TM5) respectively while the navy blue circles represent glutamine (Q). UCP2-WT had a relaxed alpha helical packing conformation **(A)**. K38Q **(B)** and K239Q **(C)** had similar loose helix packing but the conformations were slightly less relaxed than the native protein. The helix packing conformation of K141Q was more relaxed (expanded/larger triangle) **(D)** while the DM was more densely packed (small triangle) **(E)** compared to the native protein.

5.1.3. Reconstitution of UCP2 into Membrane Vesicles

Proton transport rates for selective mutants and native UCP2 proteins were successfully measured in proteoliposomes after reconstitution. Proteins were embedded into L-α-lecithin liposomes using detergent-mediated reconstitution [57]. The sizes of protein-free liposomes were larger than proteoliposomes and one possible reason is that proteins may have induced curvature

stress on the membrane of phospholipid vesicles [82]. This curvature stress could be due to the insertion of protein hydrophobic helices into the membrane bilayer which created a wedge that distorted the structure of the phospholipid membrane. In turn, this distortion may be compensated for by allowing the phospholipid head groups around the proteins to become tightly packed or released from the bilayer, which could lead to decreased liposome size [82].

Monodisperse size distribution of liposomes is preferred for ion transport experiments to ensure reliability and reproducibility of experimental results. In this study, monodisperse size distributions (≤ 20% PD) were obtained for the proteoliposomes of UCP2-WT, K38Q, and K239Q, while a polydisperse distribution of liposome sizes (≥ 20 %PD) were observed for K141Q and some of the protein-free liposomes (Table 5). A polydisperse size distribution may form due to several factors such as: type of phospholipids used, length of incubation with polysterene beads, and temperature [57]. In this particular experiment, the suspected source of polydisperse populations was during the removal of external SPQ with sephadex. After the second Biobead incubation, relatively monodisperse liposomes were produced. On the other hand, polydisperse liposomes were later observed after passing the formed vesicles through a sephadex gel filtration column. This could be due to the interaction between the phospholipids and the gel surface which led to lipid retention and increased the size distribution of liposomes [89]. Therefore, decreasing the amount of sephadex may eliminate this problem in future studies. In all, each UCP2 protein was successfully reconstituted into lipid vesicles and exhibited proton transport and ATP binding activity as discussed in the following sections.

5.1.4. Interpretation of Proton Transport Activity in UCP2

Conserved amino acid residues in protein families or homologues often imply an evolutionary significance for the residues in the structure and or function of these proteins [90]. The conserved lysine residues in the matrix network of UCP2 are suggested to participate in a salt bridge interaction with oppositely charged aspartate residues to enable the transport of substrates (ions) through the protein [42, 43]. Therefore, it was hypothesized that mutating the lysine residues to glutamine would destabilize the salt bridge network due to the loss of the positive charge on the lysine residue.

Despite the structural similarity between the UCP2 and mutant proteins, the proton transport and nucleotide binding properties differed for each protein as was expected. The proton transport activity of UCP2 was higher than the mutants (Table 7). Interestingly, the proton transport rate of UCP2 was higher than previously observed for UCP2 isolated from bacterial membranes [79]. This high transport rate could be partly due to the decreased helical packing for UCP2 monomer purified in this study. In a previous study, higher transport rates were observed for UCP1, 2, and 5 after reconstituting into vesicles containing cardiolipin. Similarly, the CD spectra and molar elliptic ratios identified a less dense helical packing conformation for the proteins and it was suggested that cardiolipin might affect the degree of helical packing that may in part, increase proton conductance in UCPs [7, 68, 79]. Based on this observation, the monomeric form of UCP2 isolated in this study may have maintained its loosely packed helical conformation in liposomes which enabled higher proton transport rates for the protein. To confirm this hypothesis, UCP2 conformation in phospholipid vesicles must be measured with far-UV CD.

In the presence of 500 μM ATP, the proton transport rate of UCP2-WT decreased by 14% compared to the uninhibited proton flux. This percent decrease in proton transport rate was less than the inhibition of proton flux previously shown for UCP2 [7]. Therefore, inhibition experiments for all UCP2 proteins needs to be repeated and reassessed to confirm the observed rates are not due to artifacts in reconstituted vesicles. A higher degree of inhibition can be achieved by trapping ATP inside the proteoliposome and adding ATP externally to the assay [7]. In addition, by comparing the inhibition of proton transport by ATP on both sides of the membrane with the inhibition by external ATP addition, the orientation of the proteins can also be determined [7].

Unlike the wild type, K38Q and K239Q had similar transport rates that were ~35% less than the wildtype. Coincidentally, both proteins had relatively identical conformations but the helices were more densely packed in comparison to the native protein. Mutating both amino acid residues (DM) induced a more dense helix packing and a transport rate that was 71% less than the native protein. UCPs with a dense helical packing has been shown to have decreased transport rates compared to its relaxed conformation when reconstituted into cardiolipin containing vesicles [7]. The differences in helical packing and proton transport rate for these proteins imply that a change in the microenvironment of the glutamine residues may have affected UCP2's ability to induce a helical packing conformation that may have partly influenced UCP2 proton transport activity. Therefore, K38 and K239 amino acids may affect the proton transport and possible helical packing of UCP2 by participating in the matrix salt bridge network.

Despite the similarities in structure and proton transport activity of K38Q and K239Q, both proteins had distinct degrees of proton transport inhibition by ATP (Table 7). The proton

transport rates of K239Q and DM decreased by < 4% while K38Q proton flux decreased by 38% in presence of ATP. Due to the close proximity of the ATP binding site and matrix network, these results imply that K38Q, K239Q and DM may have altered the microenvironment of the arginine residues that bind ATP in the protein cavity (Figure 7). In the case of K38Q, this change may have stabilized the ATP bound state more effectively than K239Q and DM proteins.

K141Q had the most relaxed helical conformation and a proton flux that was ~70% less than the wild type but similar to the DM. Therefore, K141Q seems to have an effect on proton transport rate that was similar to the loss of two lysine residues (K38 and K239) in the matrix salt bridge network. The role of K141 in FA-mediated transport activity was also detected in a mutagenic study conducted by Berardi and Chou [91] where the mutation of K141 to threonine decreased the FA-mediated proton transport of UCP2 by more than 20%. It was also proposed that K141could stabilize the carboxylate anion of the fatty acid when bound to UCP2 [91]. In spite of this new observation, the rate of proton transport for K141Q only decreased by ~7% in the presence of ATP. This implies K141Q mutation may have affected the local environment of the nucleotide binding arginine residues due to the absence of the salt bridge interaction involving K141. In all, the results obtained in this thesis project indicate that changing lysine to glutamine in the matrix network affected the degree of helical packing and altered the proton transport property of UCP2 in the presence and absence of purine nucleotide. These observed changes in structure and ion transport activity could be due to the loss of salt bridge interactions in the matrix network proposed to be involved in the ion transport mechanism of UCP2.

5.2. Conclusion and Future Studies

Despite the discovery of UCP homologues between 1970 and early 2000's, the mechanism of ion transport in these proteins remains poorly understood. To provide an insight into the mechanism of ion transport in UCP2, the positively charged lysine residues in its matrix salt bridge network were investigated for their effect on proton transport and nucleotide binding activity of the protein. As expected, mutating the K38, K141, and K239 to glutamine induced a local conformational change in the helical packing and decreased transport rates compared to UCP2-WT. Similarly, the K38Q/K239Q (DM) had a densely packed helical conformation and lower transport rate compared to the wild type. Of these mutations K141Q and DM had the most influence (decrease) on the rate of proton transport in the native protein. Inhibition studies indicated that proton transport rates of the mutants and wild type proteins were inhibited to varying extents. The proton transport rate of K38Q was the most inhibited by ATP, followed by UCP2-WT, K141Q, K239Q, and DM. These results suggest that the change in the microenvironment of each lysine residue can play a role in the conformational change of the native protein and the affinity for the inhibitor. However, additional experiments must be performed to confirm the observed proton transport rates in the presence of ATP. Overall, these lysines form salt bridges with oppositely charged aspartate residues in the matrix network of UCP2 and possibly induce local conformational changes in the protein that impact proton transport and nucleotide inhibition of UCP2. Further studies could be performed to confirm the proposed mechanism. These studies include far-UV CD measurements of the mutants and native protein in reconstituted vesicles, as well as using far and near-UV CD to measure the effect of ATP binding on the structure of UCP2 and its mutants. Previous experiments have shown that cardiolipin can affect the structure and ion transport activity of UCPs. Hence, the impact of

cardiolipin on the proton and anion transport activity and structure of UCP2 mutants in reconstituted liposome can be measured in future studies. Finally, the charged pair interactions can be mutated (*e.g.* K38Q/D236N, K141Q/D35N and K239Q/D138N) to study the effect on ion transport activity of UCP2. In conclusion, this study provided experimental evidence that indicates the importance of lysine residues in the salt bridge matrix network on the uncoupling mechanism of proton transport mediated by UCP2. In turn, understanding the mechanism of proton transport in UCP2 could improve the development of therapeutic agents for deleterious physiological conditions associated with UCP2 activity such as type II diabetes and cancer [9].

REFERENCES

1. Alberts, B., Johnson, A., Lewis, J., Raff, M., Roberts, K., and Walter, P. (2008). Molecular Biology of the Cell, 5th Ed, Chapter 14: Energy Conversion: Mitochondria and Chloroplasts. Garland Science, New York.

2. Kühlbrandt, W. (2015). Structure and function of mitochondrial membrane protein complexes. *BMC Biology*, *13*(1), 89.

3. Voet, D., and Voet, J. G. (2011) Biochemistry, 4th Ed, Chapter 22: Electron Transport and Oxidative Phosphorylation. John Wiley and Sons, Inc., NJ, USA.

4. Scheffler, E.I.,(1999). Mitochondria. Chapter 3: Structure and Morphology. Wiley-Liss, Inc, NY, USA.

5. Pfeiffer, K., Gohil, V., Stuart, R. A., Hunte, C., Brandt, U., Greenberg, M. L., & Schägger, H. (2003). Cardiolipin Stabilizes Respiratory Chain Supercomplexes. *Journal of Biological Chemistry*, *278*(52), 52873–52880.

6. Eble, K. S., Coleman, W. B., Hantgan, R. R., and Cunningham, C. C. (1990) Tightly associated cardiolipin in the bovine heart mitochondrial ATP synthase as analyzed by ^{31}P nuclear magnetic resonance spectroscopy. *J. Biol. Chem*. 265, 19434-19440.

7. Hoang, T., Smith, M. D., & Jelokhani-Niaraki, M. (2012). Toward understanding the mechanism of ion transport activity of neuronal uncoupling proteins UCP2, UCP4, and UCP5. *Biochemistry*, *51*, 4004–4014.

8. Lodish, H., Berk, A., Zipursky, S. L., Matsudaira, P., Baltimore, D., Darnell, J. (2000) Molecular Cell Biology, 4th Ed. Section 16.2, Electron Transport and Oxidative Phosphorylation. New York: W. H. Freeman.

9. Echtay, K. S. (2007). Mitochondrial uncoupling proteins--what is their physiological role? *Free Radical Biology & Medicine*, *43*(10), 1351–71.

10. Foster, D.O., and Frydman, M. L. (1979). Tissue distribution of cold-induced thermogenesis in conscious warm- or cold-adapted rats: the dominant role of brown adipose tissue. *J. Physiol. and Pharmacol. 57*, 257-270.

11. Nicholls DG, Locke RM. (1984). Thermogenic mechanisms in brown fat. *Physiol Rev.* 64, 1–64.

12. Nicholls, D. G. (1974). Hamster brown adipose tissue mitochondria: the control of respiration and the proton electrochemical potential by possible physiological effectors of the proton conductance of the inner membrane. *Eur. J. Biochem*., 49, 573–583

13. Heaton, G. M., Wagebvoord, R. J., Kemp, A., and Nicholls, D. G. (1978). Brown adipose tissue mitochondria: photoaffinity labelling of the regulatory site for energy dissipation. *J. Biochem.* 82, 515 – 521.

14. Locke, R. M., Ria, E., Scott, I. D., Nicholls, D. G. (1982). The acute regulation of mitochondrial proton conductance in cell and mitohchondria from brown fat of cold- and warm-adapted guinea-pigs. *Eur. J. Biochem.* 123, 373-380.

15. Klingenberg, M. and Huang, S. G.(1999). Structure and function of the uncoupling protein from brown adipose tissue. *Biochim. Biophys. Acta* 1415, 271–296.

16. Krauss, S., Zhang, C.-Y., & Lowell, B. B. (2005). The mitochondrial uncoupling-protein homologues. *Nature Reviews. Molecular Cell Biology*, 6 248–261.

17. Himms-Hagen, J. (1984). Thermogenesis in brown adipose tissue as an energy buffer. Implications for obesity. *N. Engl. J. Med*. 311,1549 -1558.

18. Fleury, C., Neverova, M., Collins, S., Raimbault, S., Champigny, O., Levi-Meyrueis, C., Bouillaud, F., Seldin, M. F., Surwit, R. S., Ricquier, D. and Warden, C. H. (1997). Uncoupling protein-2: a novel gene linked to obesity and hyperinsulinemia. *Nature Genet.* 15,269 -273.

19. Nègre-Salvayre, A., Hirtz, C., Carrera, G., Cazenave, R., Troly, M., Salvayre, R., Pénicaud, L. and Casteilla, L. (1997). A role for uncoupling protein-2 as a regulator of mitochondrial hydrogen peroxide generation. *FASEB J.* 11, 809 -815.

20. Zhang, C., Baffy, G., Perret, P., Krauss, S., Peroni, O., Grujic, D., Hagen, T., Vidal-Puig, A. J., Boss, O., Kim, Y., Zheng, X. X., Wheeler, M. B., Shulman, G. I., Chan, C. B. and Lowell, B. B. (2001). Uncoupling protein-2 negatively regulates insulin secretion and is a major link between obesity, beta cell dysfunction and type 2 diabetes. Cell 105,745 -755.

21. Boss, O., Samec., Paoloni-Giacobino, A., Rossier, C., Dulloo, A., Seydoux, J., Muzzin, P. and Giacobino, J., P. (1997). Uncoupling protein-3: a new member of the mitochondrial carrier family with tissue-specific expression. *FEBS Lett.* 408, 39-42.

22. Cioffi, F., Senese, R., Lange, P. De, Goglia, F., Lanni, A., Lombardi, A.,Biologiche, S. (2009). Uncoupling proteins : A complex journey to function discovery, 417–428.

23. Sanchis, D., Fleury, C., Chomiki, N, Goubern, M., Huang, Q., Neverova, M., Gregoire, F., Easlick, J., Raimbault, S., Levi-Meyrueis, C., Miroux, B., Collins, S., Seldin, M., Richard, D., Warden, C., Bouillaud, F., Ricquier,D (1998). BMCP1, a novel mitochondrial carrier with high expression in the central nervous system of humans and rodents, and respiration un- coupling activity in recombinant yeast. *J. Biol. Chem.* 273, 34611–34615.

24. Mao, W., Yu, X. X., Zhong, A., Li, W., Brush, J., Sherwood, S. W., Adams, S. H., Pan, G. (1999). UCP4, a novel brain-specific mitochondrial protein that reduces membrane potential in mammalian cells. *FEBS Lett*. 443, 326–330.

25. Carpenter, E. P., Beis, K., Cameron, A. D., & Iwata, S. (2008). Overcoming the challenges of membrane protein crystallography. Current Opinion in Structural Biology, 18(5), 581–586. http://doi.org/10.1016/j.sbi.2008.07.001.

26. Berardi, M. J., Shih, W. M., Harrison, S. C., & Chou, J. J. (2011). Mitochondrial uncoupling protein 2 structure determined by NMR molecular fragment searching. *Nature*, *476*(7358), 109–13.

27. Robinson, A. J., Overy, C., & Kunji, E. R. S. (2008). The mechanism of transport by mitochondrial carriers based on analysis of symmetry. *Proceedings of the National Academy of Sciences of the United States of America*, 105(46), 17766–17771.

28. Pebay-Peyroula, E., Dahout-Gonzalez, C., Kahn, R., Trézéguet, V., Lauquin, G. J.-M., & Brandolin, G. (2003). Structure of mitochondrial ADP/ATP carrier in complex with carboxyatractyloside. *Nature, 426*, 39–44.

29. Arsenijevic, D., Onuma, H., Pecqueur, C., Raimbault, S., Manning, B. S., Miroux, B., Couplan, E., Alves-Guerra, M. C., Goubern, M., Surwit, R., Bouillaud, F., Richard, D., Collins, S. and Ricquier, D. (2000). Disruption of the uncoupling protein-2 gene in mice reveals a role in immunity and reactive oxygen species production. *Nature Genet*. 26, 435-439.

30. Casteilla, L., Rigoulet, M., & Pénicaud, L. (2001). Mitochondrial ROS metabolism: modulation by uncoupling proteins. *IUBMB Life*, 52(3-5), 181–8.

31. Arsenijevic, D., Onuma, H., Pecqueur, C., Raimbault, S., Manning, B. S., Couplan, E., Ricquier, D. (2000). Disruption of the uncoupling protein-2 gene in mice reveals a role in immunity and reactive oxygen species production, 26, 435–439.

32. Emre, Y., & Nübel, T. (2010). Uncoupling protein UCP2: When mitochondrial activity meets immunity. *FEBS Letters*, *584*(8), 1437–1442.

33. Jezek, P., Engstová, H., Zácková, M., Vercesi, A. E., Costa, A. D. T., Arruda, P. and Garlid, K. D. (1998). Fatty acid cycling mechanism and mitochondrial uncoupling proteins. Biochim. Biophys. Acta 1365,319 -327.

34. Winkler, E., and Klingenberg M. (1994). Effect of fatty acids on H^+ transport activity of the reconstituted uncoupling protein. *J Biol Chem*, 269, 2508 – 2515.

35. Fedorenko, A., Lishko, P. V., and Kirichok, Y. (2012) Mechanism of fatty-acid-dependent UCP1 uncoupling in brown fat mitochondria. Cell 151, 400–413.

36. Chouchani, E. T., Kazak, L., Jedrychowski, M. P., Lu, G. Z., Erickson, B. K., Szpyt, J., Spiegelman, B. M. (2016). Mitochondrial ROS regulate thermogenic energy expenditure and sulfenylation of UCP1. *Nature*, *532*(7597), 112–6. doi:10.1038/nature17399.

37. Klingenberg, M., & Echtay, K. S. (2001). Uncoupling proteins: The issues from a biochemist point of view. *Biochimica et Biophysica Acta - Bioenergetics*, *1504*, 128–143. doi:10.1016/S0005-2728(00)00242-5.

38. Jezek, P., & Garlid, K. D. (1990). New substrates and competitive inhibitors of the Cl- translocating pathway of the uncoupling protein of brown adipose tissue mitochondria. *Journal of Biological Chemistry*, *265*(31), 19303–19311.

39. Hoang, T., Matovic, T., Parker, J., Smith, M. D., & Jelokhani-Niaraki, M. (2015). Role of positively charged residues of the second transmembrane domain in the ion transport activity and conformation of human uncoupling protein-2. *Biochemistry*, *54*(14), 2303–2313.

40. Nelson, D. R., Felix, C. M., & Swanson, J. M. (1998). Highly conserved charge-pair networks in the mitochondrial carrier family. *Journal of Molecular Biology*, *277*, 285–308.

41. Pebay-Peyroula, E., Dahout-Gonzalez, C., Kahn, R., Trézéguet, V., Lauquin, G. J.-M., & Brandolin, G. (2003). Structure of mitochondrial ADP/ATP carrier in complex with carboxyatractyloside. *Nature*, *426*, 39–44.

42. Robinson, A. J., & Kunji, E. R. S. (2006). Mitochondrial carriers in the cytoplasmic state have a common substrate binding site. *Proceedings of the National Academy of Sciences of the United States of America*, 103(8), 2617–22.

43. Miniero, D. V., Cappello, A. R., Curcio, R., Ludovico, A., Daddabbo, L., Stipani, I., Palmieri, F. (2011). Functional and structural role of amino acid residues in the matrix -α-helices, termini and cytosolic loops of the bovine mitochondrial oxoglutarate carrier. *Biochimica et Biophysica Acta - Bioenergetics*, 1807(3), 302–310.

44. Ruprecht, J. J., Hellawell, A. M., Harding, M., Crichton, P. G., McCoy, A. J., Kunji, Edmund R S, & Kunji, E. R. S. (2014). Structures of yeast mitochondrial ADP/ATP carriers support a domain-based alternating-access transport mechanism. *Proceedings of the National Academy of Sciences of the United States of America*, 111(4), 426–34.

45. Kursula, I., Partanen, S., Lambeir, A. M., & Wierenga, R. K. (2002). The importance of the conserved Arg191-Asp227 salt bridge of triosephosphate isomerase for folding, stability, and catalysis. *FEBS Letters*, *518*(1-3), 39–42.

46. Garlid, K. D., Orosz, D. E., Modrianský, M., Vassanelli, S., & Jezek, P. (1996). On the mechanism of fatty acid-induced proton transport by mitochondrial uncoupling protein. The Journal of Biological Chemistry, 271(5), 2615–2620.

47. Ho, S. N., Ho, S. N., Hunt, H. D., Hunt, H. D., Horton, R. M., Horton, R. M., Pease, L. R. (1989). Site-directed mutagenesis by overlap extension using the polymerase chain reaction. *Gene*, *77*, 51–9.

48. Heckman KL, Pease LR. (2007) Gene Splicing and Mutagenesis by PCR-Driven Overlap Extension. Nat Protoc. 2, 924-923.

49. Natale, P., Bryser, T., & Driessen, A. J. M. (2008). Sec- and Tat-mediated protein secretion across the bacterial cytoplasmic membrane-Distinct translocases and mechanisms. *Biochimica et Biophysica Acta - Biomembranes*, *1778*(9), 1735–1756.

50. Lei, S. P., Lin, H. C., Wang, S. S., & Wilcox, G. (1988). Characterization of the Erwinia-Carotovora Pel-a Gene and Its Product Pectate Lyase A. *Gene (Amsterdam)*, *62*(1), 159–16.

51. Sambrook J, Russel DW. (2001) Molecular Cloning: A Laboratory Manual, Cold Spring Harbor Laboratory Press, Cold Spring Harbor, NY, pp 1.63-1.70.

52. Studier, F. W. (2005). Protein production by auto-induction in high density shaking cultures. *Protein Expression and Purification*, *41*, 207–234.

53. Shapiro, a L., Viñuela, E., & Maizel, J. V. (1967). Molecular weight estimation of polypeptide chains by electrophoresis in SDS-polyacrylamide gels. *Biochemical and Biophysical Research Communications*, *28*(5), 815–820.

54. Wilson, K., and Walker, J. (2005). Principles and Techniques of Biochemistry and Molecular Biology, 6th Ed. Chapter 10: Electrophoretic Techniques. Cambridge University Press. New York.

55. Mahmood, T., & Yang, P.-C. (2012). Western Blot: Technique, Theory, and Trouble Shooting. *North American Journal of Medical Sciences*, *4*(9), 429–434.

56. Luckey, M. (2008). Membrane Structural Biology: With Biochemical and Biophysical Foundations, 1st Ed. Chapter 1: Introduction and Chapter 3: Tools for Studying Membrane Components: Detergents and Model Systems. Cambridge University Press. New York.

57. Rigaud, J. L., Pitard, B., & Levy, D. (1995). Reconstitution of membrane proteins into liposomes: application to energy-transducing membrane proteins. *Biochimica et Biophysica Acta*, *1231*, 223–246.

58. Szoka, F., & Papahadjopoulos, D. (1978). Procedure for preparation of liposomes with large internal aqueous space and high capture by reverse-phase evaporation. Proceedings of the National Academy of Sciences of the United States of America, 75(9), 4194–4198.

59. Lapinski, M. M., Castro-Forero, A., Greiner, A. J., Ofoli, R. Y.,& Blanchard, G. J. (2007). Comparison of liposomes formed by sonication and extrusion: Rotational and translational diffusion of an embedded chro89mophore. *Langmuir*, *23*(23), 11677–11683.

60. Berne, J., B., and Pecora, R. (2000). Dynamic Light Scattering: With Application to Chemistry, Biology, and Physics. Dover Publications Inc. New York.

61. Lorber, B., Fischer, F., Bailly, M., Roy, H., & Kern, D. (2012). Protein analysis by dynamic light scattering: Methods and techniques for students. *Biochemistry and Molecular Biology Education*, *40*(6), 372–382.

62. Khurshid, S., Saridakis, E., Govada, L., Chayen., E., N. (2014). Porous Nucleating Agents for Protein Crystallization. *Nature Protocols,* 9, 1621-1633.

63. Kelly, S. M., & Price, N. C. (2000). The use of circular dichroism in the investigation of protein structure and function. *Current Protein & Peptide Science*, *1*, 349–384.

64. Bright, V. F. (1988). Bioanalytical Applications of Fluorescence Spectroscopy. *Analytical Chemistry*, 60 (18), 1031A-1039A.

65. Lakowicz, J. R. (2006). Principles of fluorescence spectroscopy, 3rd Edition. Chapter 1: Introduction to Fluorescence. Chapter 2: Instrumentation for Fluorescence Spectroscopy. Springer, New York, USA.

66. Orosz, D. E., & Garlid, K. D., (1993) A sensitive new fluorescence assay for measuring proton transport across liposomal membranes. *Anal Biochem*. 210, 7-15.

67. Bregestovski, P., Waseem, T., & Mukhtarov, M. (2009). Genetically encoded optical sensors for monitoring of intracellular chloride and chloride-selective channel activity. *Frontiers in Molecular Neuroscience*, 2, 15.

68. Hoang, T., Smith, M. D., & Jelokhani-Niaraki, M. (2013). Expression, folding, and proton transport activity of human uncoupling protein-1 (ucp1) in lipid membranes. *Journal of Biological Chemistry*, *288*(51), 36244–36258.

69. Promega Corporation: Wizard® SV Gel and PCR Clean-Up System Technical Bulletin.

70. E.Z.N.A. (2012). Gel Extraction Kit Instruction Manual.

71. Qiagen: HotStar HiFidelity PCR Handbook.

72. Sambrook J, Russel DW. (2001) Molecular Cloning: A Laboratory Manual, Cold Spring Harbor Laboratory Press, Cold Spring Harbor, NY, pp 1.63-1.70.

73. Bornhorst, J. A., & Falke, J. J. (2000). [16] Purification of Proteins Using Polyhistidine Affinity Tags. Methods in Enzymology, 326, 245–254.

74. Whitmore, L., and Wallace, B. A. (2004) Dichroweb, an online server for protein secondary structure analyses from circular dichroism spectroscopic data. *Nucleic Acids Res.* 32, 668–673.

75. Lees, J. G., Miles, A. J., Wien, F., and Wallace, B. A. (2006) A reference database for circular dichroism spectroscopy covering fold and secondary structure space. *Bioinformatics* **22**, 1955–1962.

76. Altschul S.F., Gish W., Miller W., Myers E.W. and Lipman D.J. (1990) Basic local alignment search tool. J. Mol. Biol. 215: 403-410.

77. Stratagene. (2005). BL21-CodonPlus Competent Cells Instruction Manual.

78. Singh, P., Sharma, L., Kulothungan S. R., Adkar B. V., Prajapati R, S.,Syed Ali, P. S., Krishnan, B., and Varadarajan, R. (2013) Effect of Signal Peptide on Stability and Folding of Escherichia coli Thioredoxin. *PLOS ONE* 8(5): 63442.

79. Hoang, T., Kuljanin, M., Smith, M. D., and Jelokhani-Niaraki, M. (2015). A biophysical study on molecular physiology of the uncoupling proteins of the central nervous system. *Bioscience Reports*, *35*(4), 00226.

80. Ryan, B. J., & Henehan, G. T. (2013). Overview of approaches to preventing and avoiding proteolysis during expression and purification of proteins. *Current Protocols in Protein Science*, 71.

81. Ivanova, M. V., Hoang, T., McSorley, F. R., Krnac, G., Smith, M. D., & Jelokhani-Niaraki, M. (2010). A comparative study on conformation and ligand binding of the neuronal uncoupling proteins. *Biochemistry*, *49*, 512–521.

82. Zimmerberg, J.; Kozlov, M. M. How Proteins Produce Cellular Membrane Curvature. Nat. Rev. Mol. Cell Biol. 2006, 7 (1), 9–19.

83. Malvern Instruments. (2011). Dynamic Light Scattering Common Terms Defined. *Malvern Guides*, 1–6.

84. Mus-Veteau, I. (2010) Heterologous expression of membrane proteins for structural analysis. Methods Mol. Biol. 601, 1–16.

85. Singh, A.; Upadhyay, V.; Upadhyay, A. K.; Singh, S. M.; Panda, A. K. Protein Recovery from Inclusion Bodies of Escherichia Coli Using Mild Solubilization Process. *Microb. Cell Fact.* **2015**, *14* (1), 41.

86. Kalipatnapu, S., & Chattopadhyay, A. (2005). Membrane protein solubilization: recent advances and challenges in solubilization of serotonin1A receptors. *IUBMB Life*, *57*(7), 501-507.

87. Lee, Y., Willers, C., Kunji, E. R. S., & Crichton, P. G. (2015). Uncoupling protein 1 binds one nucleotide per monomer and is stabilized by tightly bound cardiolipin. *Proceedings of the National Academy of Sciences of the United States of America*, *112*(22), 6973–6978.

88. Qiagen. (2003). A handbook for high-level expression and purification of 6xHis-tagged proteins. The QIA expressionist.

89. Ruysschaert, T.; Marque, A.; Duteyrat, J.-L.; Lesieur, S.; Winterhalter, M.; Fournier, D. Liposome Retention in Size Exclusion Chromatography. BMC Biotechnol. 2005, 5, 11.

90. Majewski, J., & Ott, J. (2003). Amino acid substitutions in the human genome: Evolutionary implications of single nucleotide polymorphisms. *Gene*, *305*(2), 167–173.

91. Zhu, R., Rupprecht, A., Ebner, A., Haselgrübler, T., Gruber, H. J., Hinterdorfer, P., & Pohl, E. E. (2012). Study of Nucleotide Binding to the Uncoupling Protein 1 using Atomic Force Microscopy. *Biophysical Journal*, *102*(3), 607a.

92. Nury, H., Dahout-Gonzalez, C., Trézéguet, V., Lauquin, G., Brandolin, G., and Pebay-Peyroula, E. (2005) Structural basis for lipid-mediated interactions between mitochondrial ADP/ATP carrier monomers. *FEBS Lett*. 579, 6031–6036.

93. Berardi MJ, Chou JJ. Fatty Acid Flippase Activity Of UCP2 Is Essential For Its Proton Transport In Mitochondria. *Cell metabolism*. 2014;20(3):541-552.

94. The PyMOL Molecular Graphics System, Version 1.8 Schrödinger, LLC.

95. Sievers F, Wilm A, Dineen DG, Gibson TJ, Karplus K, Li W, Lopez R, McWilliam H,Remmert M, Söding J, Thompson JD, Higgins D. (2011) Fast, scalable generation of high-quality protein multiple sequence alignments using Clustal Omega. *Molecular Systems Biology*, 7, 539.

APPENDICES

Appendix 1 - Sequence Alignment of UCP Homologues and ADP/ATP carrier

Figure A1: Sequence alignment of bovine ATP/ADP 1 carrier protein (ADT1) and human uncoupling protein 1, 2, 3, 4, and 5 in Clustal O 2.1 [95]. The alignment shows the charged amino acid residues amino acids residues of the matrix salt-bridge motifs that are conserved amongst ADT1 and the UCP homologues (highlighted in yellow). The arginine residues (R88, R185, and R279) that bind purine nucleotides in UCP2 are highlighted in green. The accession numbers from protein data bank are written beside each protein.

Appendix 2 - T7 Terminator Sequenced cDNA for K38Q, K141Q, and K239Q

Homo sapiens uncoupling protein 2 (UCP2), mRNA
Sequence ID: NM_003355.2 Length: 1646 Number of Matches: 1

Range 1: 381 to 1308 GenBank Graphics Next Match

Score	Expect	Identities	Gaps	Strand
1683 bits(911)	0.0	923/928(99%)	3/928(0%)	Plus/Minu

```
Query  78    AGAAGGGAGCCTCTCGGGAAGTGCAGGCAGCCATGAGGGCTCGTTTCAGCTGCTCATAGG  137
Sbjct  1308  AGAAGGGAGCCTCTCGGGAAGTGCAGGCAGCCATGAGGGCTCGTTTCAGCTGCTCATAGG  1249
Query  138   TGACGAACATCACCACGTTCCAGGAACCCAAGCGGAGAAAGGAGGGCATGAACCCTTTGT  197
Sbjct  1248  TGACGAACATCACCACGTTCCAGGAACCCAAGCGGAGAAAGGAGGGCATGAACCCTTTGT  1189
Query  198   AGAAGGCTCGGGGCCCCTCCTTCTGGAGCATGGTAAGGGCACAGTGGCCAGCGCTACTGT  257
Sbjct  1188  AGAAGGCTCGGGGCCCCTCCTTCTGGAGCATGGTAAGGGCACAGTGGCCAGCGCTACTGT  1129
Query  258   ACTGGCCCAGGGCAGAGTTCATGTATCTCGTCTTGACCACGTCTACAGGGGAGGCGATGA  317
Sbjct  1128  ACTGGCCCAGGGCAGAGTTCATGTATCTCGTCTTGACCACGTCTACAGGGGAGGCGATGA  1069
Query  318   CAGTGGTGCAGAAGCCTGCCCCAAAGGCAGAAGTGAAGTGGCAAGGGAGGTCATCTGTCA  377
Sbjct  1068  CAGTGGTGCAGAAGCCTGCCCCAAAGGCAGAAGTGAAGTGGCAAGGGAGGTCATCTGTCA  1009
Query  378   TGAGGTTGGCTTTCAGGAGGGCATCCTTGATGAGGTCATAGGTCACCAGCTCAGCACAGT  437
Sbjct  1008  TGAGGTTGGCTTTCAGGAGGGCATCCTTGATGAGGTCATAGGTCACCAGCTCAGCACAGT  949
Query  438   TGACAATGGCATTACGAGCAACATTGGGAGAGGTCCCTTTCCAGAGGCCCCGGAACCCTT  497
Sbjct  948   TGACAATGGCATTACGAGCAACATTGGGAGAGGTCCCTTTCCAGAGGCCCCGGAACCCTT  889
Query  498   CCTCTCGGGCAATGGTCTTGTAGGCATTGACGGTGCTTTGGTATCTCCGACCACCTCCAG  557
Sbjct  888   CCTCTCGGGCAATGGTCTTGTAGGCATTGACGGTGCTTTGGTATCTCCGACCACCTCCAG  829
Query  558   CCCGGGCCTGAGCTTGGAATCGGACCTTTACCACATCCGTGGGCTGGGCCACAGCCACAG  617
Sbjct  828   CCCGGGCCTGAGCTTGGAATCGGACCTTTACCACATCCGTGGGCTGGGCCACAGCCACAG  769
Query  618   CCAGGGCACCTGTGGTGCTGCCTGCTAGGAGGCGGCTCCCAATGCTGGCATGCTCAGAGC  677
Sbjct  768   CCAGGGCACCTGTGGTGCTGCCTGCTAGGAGGCGGCTCCCAATGCTGGCATGCTCAGAGC  709
Query  678   CCTTGGTGTAGAACTGTTTGACAGAATCATACAGGCCGATGCGGACAGAGGCAAAGCTCA  737
Sbjct  708   CCTTGGTGTAGAACTGTTTGACAGAATCATACAGGCCGATGCGGACAGAGGCAAAGCTCA  649
Query  738   TTTGGCGCTGCAGGCCGGCAACCAGCCCATTGTAGAGGCTTCGGGGGCCCTCAGTACGCA  797
Sbjct  648   TTTGGCGCTGCAGGCCGGCAACCAGCCCATTGTAGAGGCTTCGGGGGCCCTCAGTACGCA  589
Query  798   CCATAGTCAGAATGGTGCCCATCACACCGCGGTACTGGGCGCTGGCTGTAGCGCGCACTG  857
Sbjct  588   CCATGGTCAGAATGGTGCCCATCACACCGCGGTACTGGGCGCTGGCTGTAGCGCGCACTG  529
Query  858   GCCCCTGACTTTCTCCTTGGATCTGTAACCGGACTTGAGCAGTATCCAGAGGAAAGGTGA  917
Sbjct  528   GCCCCTGACTTTCTCCTTGGATCTGTAACCGGACTTTAGCAGTATCCAGAGGAAAGGTGA  469
Query  918   TGAGATCTGCGATGCAGGCAGCTGTGCCAGCCC-AAGAAACTTCACAGTGGCAGTAGGGG  976
Sbjct  468   TGAGATCTGCGATGCAGGCAGCTGTGCCAGCCCCAAGAAACTTCACAGTGGCAGTAGGGG  409
Query  977   -CACATCTGTGGCCTTGA-CCCAACCAT  1002
Sbjct  408   GCACATCTGTGGCCTTGAACCCAACCAT  381
```

Figure A2-1: Sequence alignment of PCR T7 Primed K38Q (query) and hUCP2wt cDNA (subject) in NCBI nucleotide blast database. [96]

Figure A2-2: Sequence alignment of T7 terminator Primed K141 (query) and hUCP2wt cDNA (subject) in NCBI nucleotide blast database [76]

Figure A2-3: Sequence alignment of PCR T7 Terminator Primed K239Q (query) and hUCP2wt cDNA (subject) in NCBI nucleotide blast database [76].